

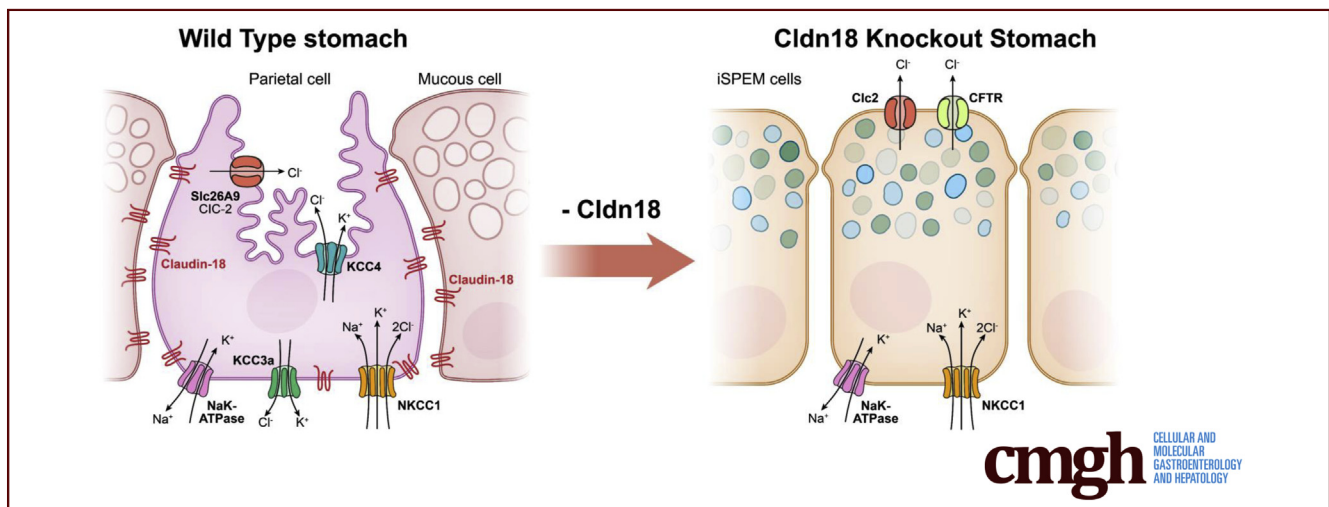
ORIGINAL RESEARCH

Claudin-18 Loss Alters Transcellular Chloride Flux but not Tight Junction Ion Selectivity in Gastric Epithelial Cells



Tyler J. Caron,^{1,3,4} Kathleen E. Scott,^{1,3,4} Nishita Sinha,¹ Sureshkumar Muthupalani,³ Mahnoor Baqai,^{1,2} Lay-Hong Ang,^{1,2} Yue Li,^{1,2} Jerrold R. Turner,^{2,5} James G. Fox,^{3,4} and Susan J. Hagen^{1,2}

¹Department of Surgery/Division of General Surgery, Beth Israel Deaconess Medical Center, Boston, Massachusetts; ²Harvard Medical School, Boston, Massachusetts; ³Division of Comparative Medicine, Massachusetts Institute of Technology, Cambridge, Massachusetts; ⁴Department of Biological Engineering, Massachusetts Institute of Technology, Cambridge, Massachusetts; and ⁵Department of Pathology, Brigham and Women's Hospital, Boston, Massachusetts



SUMMARY

Claudin-18 loss during *Helicobacter pylori* infection promotes neoplastic progression. This phenotype was not due to barrier dysfunction, because paracellular permeability was not affected by claudin-18 deletion but may be secondary to transcellular anion transporter expression/function in the absence of claudin-18.

BACKGROUND & AIMS: Tight junctions form a barrier to the paracellular passage of luminal antigens. Although most tight junction proteins reside within the apical tight junction complex, claudin-18 localizes mainly to the basolateral membrane where its contribution to paracellular ion transport is undefined. Claudin-18 loss in mice results in gastric neoplasia development and tumorigenesis that may or may not be due to tight junction dysfunction. The aim here was to investigate paracellular permeability defects in stomach mucosa from claudin-18 knockout (*Cldn18*-KO) mice.

METHODS: Stomach tissue from wild-type, heterozygous, or *Cldn18*-KO mice were stripped of the external muscle layer and mounted in Ussing chambers. Transepithelial resistance, dextran 4 kDa flux, and potential difference (PD) were calculated from the chambered tissues after identifying differences in tissue

histopathology that were used to normalize these measurements. Marker expression for claudins and ion transporters were investigated by transcriptomic and immunostaining analysis.

RESULTS: No paracellular permeability defects were evident in stomach mucosa from *Cldn18*-KO mice. RNAseq identified changes in 4 claudins from *Cldn18*-KO mice, particularly the up-regulation of claudin-2. Although claudin-2 localized to tight junctions in cells at the base of gastric glands, its presence did not contribute overall to mucosal permeability. Stomach tissue from *Cldn18*-KO mice also had no PD versus a lumen-negative PD in tissues from wild-type mice. This difference resulted from changes in transcellular Cl⁻ permeability with the down-regulation of Cl⁻ loading and Cl⁻ secreting anion transporters.

CONCLUSIONS: Our findings suggest that *Cldn18*-KO has no effect on tight junction permeability in the stomach from adult mice but rather affects anion permeability. The phenotype in these mice may thus be secondary to transcellular anion transporter expression/function in the absence of claudin-18. (*Cell Mol Gastroenterol Hepatol* 2021;11:783-801; <https://doi.org/10.1016/j.jcmgh.2020.10.005>)

Keywords: Claudin-2; Paracellular Permeability; Genomic Profile; Ussing Chambers; RNAseq; Gastric Cancer.

One essential function of epithelial cells is to regulate ion transport between apical (mucosal) and basolateral (serosal) surfaces via transcellular and paracellular pathways. Whereas the transcellular pathway requires specific transporters that move ions into (ion loading) and out (ion secretion) of cells, the specificity and selectivity of paracellular transport occur at the apical tight junction complex.¹⁻⁵ The main contributors to selective permeability at tight junctions are claudin molecules, a family of membrane-bound, tetraspanning, and pore-forming proteins.⁶⁻⁹ There are currently 27 annotated members of the claudin family in rodents; each is thought to confer a unique selectivity to the passage of charged and uncharged solutes. Claudins are expressed in a tissue-dependent manner; in a given tissue the dynamics of paracellular permeability are largely defined by the distinct combination of expressed claudins.^{2,7,10}

In the human and mouse stomach, the major claudin molecule expressed in epithelial cells is claudin-18. Claudin-18 has 2 isoforms; *Cldn18A2.1* is primarily expressed in the stomach, and *Cldn18A1.1* is expressed in the lung. A previous study of mice lacking the stomach isoform (*stCldn18-KO*) reported increased mucosal to serosal H⁺ flux and concluded that claudin-18 forms a paracellular barrier to cation permeation at tight junctions.¹¹ Consistent with this, transmucosal Na⁺ (cation) and Cl⁻ (anion) permeabilities were also increased in *stCldn18-KO* mice.¹¹ This increased cation and anion permeability was proposed to be caused by the up-regulation of claudin-2 and claudin-7, respectively.¹¹ Cation permeability defects at tight junctions, promoting inflammation and mucosal injury that do not resolve, were thought to cause spasmodic polypeptide-expressing metaplasia¹¹ and were proposed to account for the development of gastric tumors in *stCldn18-KO* mice.¹² Permeability defects also occurred at tight junctions in cultured cells incubated with *Helicobacter pylori*,¹³ and tight junction dysfunction is thought to be a risk factor for *H pylori*-induced gastric cancer development.¹⁴

Although tight junction proteins typically reside within the apical tight junction complex, we showed using super-resolution microscopy techniques in archived formalin-fixed paraffin-embedded (FFPE) tissues that stomach-specific claudin-18A2.1 localized mainly to the basolateral membrane of gastric epithelial cells.¹⁵ It was previously demonstrated that *Cldn-18A1.1* (lung isoform), which is not normally expressed in the adult stomach, was highly expressed in adult *stCldn18-KO* mice and localized to tight junctions.¹¹ Because the lung isoform was highly expressed at tight junctions, it was unclear to us why a cation leak occurred in *stCldn18-KO* mice unless the lung and stomach isoforms function differently. It was also demonstrated that gastric tissues from *stCldn18-KO* mice were actively proliferating along the gland base, which caused a significant increase in the number of cells lining the gastric glands.¹¹ We observed a similar pattern of proliferation and cellular hyperplasia in mice lacking both lung and stomach isoforms of claudin-18 (*Cldn18-KO* mice).¹⁵ Because an increase in the number of cells, which increases mucosal surface area, is known to affect tissue conductance, it was unclear whether the transepithelial resistance (TER) and

permeability data reported for *stCldn18-KO* mice¹¹ were due to cellular hyperplasia or reflected differences in tight junction function, per se.


Therefore, the present study was designed to explore the regulation of permeability changes in *Cldn18-KO* mice, which show progressive neoplasia development with significant premalignant lesions in the gastric mucosa by 7 weeks after birth.¹⁵ This model is clinically relevant, because the stomach mucosa from gastric cancer patients without claudin-18 have neither stomach nor lung isoforms.^{16,17} We demonstrate here that *Cldn18-KO* has no effect on gastric paracellular permeability when the measured TER, dilution potential, and paracellular flux data are corrected for surface area and mucosal cell number. *Cldn18-KO* mice had increased expression of claudin-2, which was mainly localized to cells at the base of gastric glands, but despite this result had no alterations in ion conductance or paracellular permeability. Furthermore, tissues from *Cldn18-KO* mice showed considerable differences in Cl⁻ but not Na⁺ permeability because of gastric atrophy and impairment of transcellular Cl⁻ transport. Our data suggest that adult *Cldn18-KO* mice lack significant permeability defects to cause progressive neoplasia development and gastric tumorigenesis, but instead the phenotype in these mice may thus be secondary to transcellular anion transporter expression/function in the absence of claudin-18.

Results

Cldn18 Deficiency Results in the Reorganization of Tight Junction Claudins

To determine whether the deletion of *Cldn18* affects the expression of other claudin or tight junction components, genomic profiling of the neck region from the gastric mucosa of claudin-18 wild-type (*Cldn18^{+/+}*) and *Cldn18-KO* (*Cldn18^{-/-}*) mice was done.¹⁵ Our mouse database annotated 26 of 27 rodent claudin genes (Figure 1). For claudin-18 wild-type mice, claudin gene expression could be stratified into 3 groups: (1) low (<100 normalized counts, 18/26 claudins); (2) medium (101–2000 normalized counts including *Cldn 3, 4, 7, 8, 12,* and *25*); and (3) high (>25,000 normalized counts, limited to *Cldn18*) (Figure 1A and B). Significant changes in claudin gene expression for *Cldn18-KO* mice included the down-regulation of *Cldns 8* and *15* and the up-regulation of *Cldns 2* and *23* (Figure 1C and D,

Abbreviations used in this paper: ANOVA, analysis of variance; Cldn, claudin; *Cldn18-KO* mice, claudin-18 knockout mice that are mice deficient in both stomach and lung isoforms of claudin-18; FD-4, fluorescein isothiocyanate-dextran, average molecular weight 4000; FFPE, formalin-fixed paraffin-embedded; MIT, Massachusetts Institute of Technology; NaK-ATPase, sodium (Na⁺), potassium (K⁺)-ATPase; NKCC1, sodium (Na⁺)-potassium (K⁺)-2 chloride (2 Cl⁻) cotransporter-1; PD, potential difference; SE, standard error; *stCldn18-KO* mice, claudin-18 knockout mice with the knockout directed specifically to the stomach isoform of claudin-18; TER, transepithelial resistance.

 Most current article

© 2020 The Authors. Published by Elsevier Inc. on behalf of the AGA Institute. This is an open access article under the CC BY-NC-ND license (<http://creativecommons.org/licenses/by-nc-nd/4.0/>).

2352-345X

<https://doi.org/10.1016/j.jcmgh.2020.10.005>

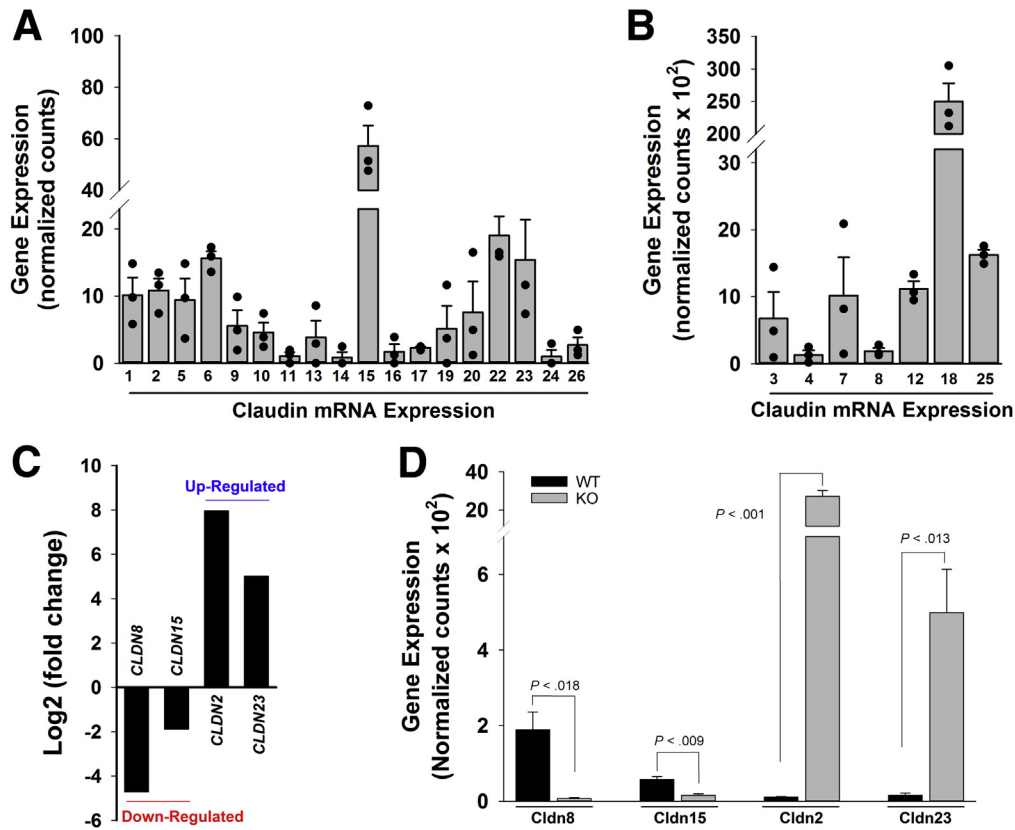


Figure 1. Gene expression changes in *Cldn18*-KO mice at 7 weeks after birth suggest an increase in cation permeability of the gastric mucosa. (A) Claudin mRNA expression in gastric epithelial cells ranges from 0 to 100 normalized counts for 18/26 of the claudin molecules. These were considered low/no-expression claudins in the stomach. (B) Claudin mRNA expression in gastric epithelial cells from 101 to 2000 normalized counts include *Cldn3*, -4, -7, -8, -12, and -25. *Cldn18* expression, which is greater than 25,000 normalized counts, was higher than any other claudin. (C and D) When compared with wild-type mice, *Cldn18*-KO mice display significant down-regulation in mRNA expression for *Cldn8* and -15 and significant up-regulation in mRNA expression for *Cldn2* and -23. Normalized gene expression data from wild-type and *Cldn18*-KO mice were generated from 3 male mice per genotype and plotted as mean \pm standard error (SE). Log₂ data for wild-type and *Cldn18*-KO mice were generated from 3 male mice per genotype and plotted as fold change with criteria of adjusted *P* value of .0001 or less as described previously.¹⁵

Table 1). Claudin-8 is barrier-enhancing, and claudins-8 and -15 form a barrier to cation permeation like claudin-18.⁷ In addition, claudin-2 forms cation channels.^{2,18} Overall, these data suggest that remodeling of tight junction claudins occurs after the deletion of *Cldn18* to facilitate a mucosa leaky to cations, particularly with the highly significant up-regulation of claudin-2. There was also significant up-regulation of tight junction associated MARVEL proteins, adherens junction, desmosome, and gap junction gene expression in *Cldn18*-KO mice (Table 1). These results likely reflect a significant increase in cell number in *Cldn18*-KO mice.¹⁵

Transepithelial Resistance and Paracellular Permeability Are Unaltered in *Cldn18*-KO Mice at 7 Weeks After Birth

Because the genomic profile from *Cldn18*-KO mice suggests a leaky mucosa, particularly to Na⁺ and other cations,

we examined barrier properties of the stomach mucosa from wild-type, heterozygous (*Cldn18*^{+/-}), and *Cldn18*-KO mice by measuring TER and the rate of mucosal to serosal dextran 4 kDa (FD-4) flux. Calculating both TER and FD-4 flux requires a measurement of the surface area of epithelial cells, which is typically assumed to be the same in each treatment.

However, because of the physical shape of the mammalian stomach, tissues from the greater curvature were unable to be stretched flat, thus causing folds in the mucosa that changed the overall mucosal length of the chambered tissue from 9 mm (calculated diameter or reservoir opening length of CHM2 Ussing chambers; World Precision Instruments, Sarasota County, FL) to about 10 mm, which was calculated from the actual length of tissues taken from the chamber after the experiment (Figure 2A-C). Although no significant difference was found in the length of tissues from wild-type, heterozygous, or *Cldn18*-KO mice (Figure 2C), we calculated TER and FD-4 flux using the correct surface areas derived from the length measurement for each tissue. In addition, the mucosa from *Cldn18*-KO mice was significantly thicker (Figure 2D-F),

Table 1. List of Gene Fold-Change (Log2) Data Associated With Epithelial Junctional Complexes in Stomach of *Cldn18*-KO Versus Wild-Type Mice at 7 Weeks After Birth

Gene designation	Log2	Significance (adjusted <i>P</i> value)	Gene name
Tight junctions			
(a) Scaffolding proteins			
Tjp1	+0.84	8.66E ⁻⁰⁴	Zonula occludins-1 (ZO-1)
Tjp2	+1.35	8.36E ⁻⁰⁹	Zonula occludins-2 (ZO-2)
Tjp3	+1.07	1.20E ⁻⁰⁵	Zonula occludins-3 (ZO-3)
Cgn	+1.49	1.05E ⁻⁰⁷	Cingulin
Mlit4	+0.78	.003	Afadin
Magi1	-0.78	.003	Membrane associated guanylate kinase-1
Magi3	+0.29	NS (0.53)	Membrane associated guanylate kinase-3
Mpdz	+0.06	NS (1.0)	Multiple PDZ domain protein (MUPP-1)
(b) Junctional adhesion molecules			
F11r	+0.18	NS (0.82)	Junctional adhesion molecule-A (JAM-A)
Jam2	-0.49	NS (0.45)	Junctional adhesion molecule-B
Jam3	-1.18	.016	Junctional adhesion molecule-C
(c) Tight junction associated MARVEL proteins (TAMPS)			
Ocln	+0.91	.0002	Occludin
Marveld2	+0.60	.05	Tricellulin
Marveld3	-0.85	NS (0.17)	MarvelD3
(d) Claudins^a			
Cldn2	+7.97	4.84E ⁻⁶¹	Claudin-2
Cldn8	-4.71	1.12E ⁻⁰⁶	Claudin-8
Cldn15	-1.89	.012	Claudin-15
Cldn23	+5.02	8.68E ⁻⁰⁹	Claudin-23
Adherens junctions			
Cdh1	+1.03	8.23E ⁻⁰⁵	E-cadherin
Ctnna1	+0.92	6.80E ⁻⁰⁴	α-catenin
Ctnna2	-0.81	NS (0.88)	β-catenin
Pvrl-1	+0.67	.0067	Nectin-1
Pvrl-2	+1.69	6.92E ⁻¹⁵	Nectin-2
Desmosomes			
Dsg2	+1.07	8.58E ⁻⁰⁶	Desmoglein 2
Gap junctions			
Gja1	+1.81	5.77E ⁻⁰⁶	Connexin-43
Gjb1	+1.07	.013	Connexin-32
Gjb2	+2.53	.001	Connexin-26
Gjc1	-1.56	1.4E ⁻⁰⁴	Connexin-45

NS, no significant difference.

^aClaudins that changed significantly are included.

containing longer glands with a greater number of cells per area¹⁵ and thus a greater surface area. To account for this difference, we measured the mucosal height from each tissue and used this figure to normalize TER and FD-4 flux measurements. It should also be noted that each tissue was also evaluated in H&E sections after the chamber experiment (Figure 2D and E) to ensure that proper nutrient and gas perfusion occurred; in a few of the tissues we ran in the Ussing chamber, poor perfusion led to a band of necrotic tissue in the center. This feature was used to exclude tissues from the study because cells in the tissue center were presumed to be nonviable. Tattering of the apical surface (Figure 2E) is a feature of the *Cldn18*-KO mouse stomach mucosa¹⁵ and not related to running tissues in the Ussing chamber.

When the data were normalized to mucosal height, there was no significant difference in TER, conductance, or luminal to basolateral FD-4 flux in *Cldn18*-KO mice (Figure 3A, C, and E). In addition, there was no effect of

gender on TER (Figure 3A; $F_{1,29} = 1.492$; $P = .223$) or on the mucosal to serosal FD-4 flux (Figure 3E; $F_{1,31} = 0.529$; $P = .752$). In contrast, when differences in mucosal height were not considered in the calculations, the results showed a significant decrease in TER, an increase in conductance (Figure 3B and D), and a significant increase in FD-4 flux (Figure 3F) in *Cldn18*-KO compared with wild-type or heterozygous mice. Hence, the results obtained by calculating TER and permeability measurements using the surface area from each individual tissue and normalizing the data to mucosal height suggest that the loss of *Cldn18* does not affect tight junction function in the ex vivo stomach at 7 weeks after birth.

Claudin-2 Protein Is Expressed in the Stomach Mucosa of Cldn18-KO Mice

The results indicating no increase in TER or paracellular permeability in *Cldn18*-KO mice were inconsistent with

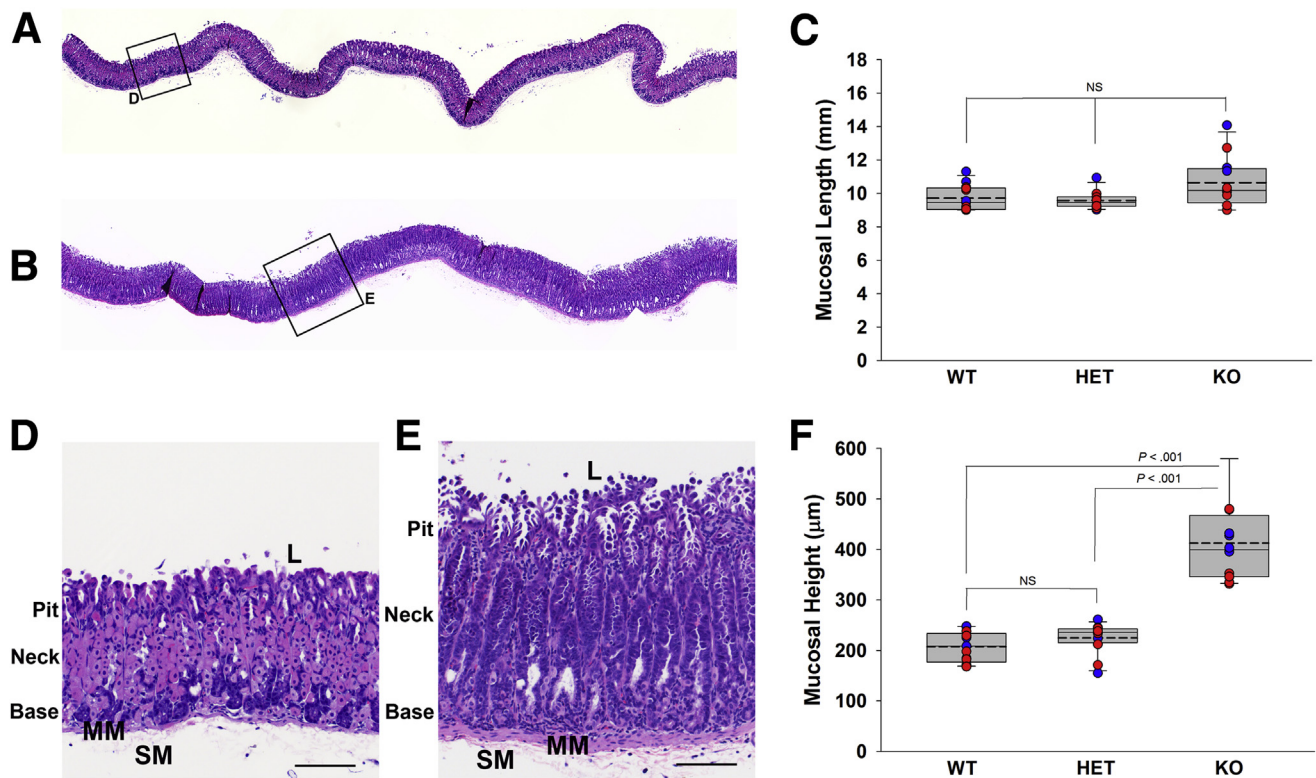


Figure 2. Gastric mucosal length and thickness differ in chambered tissues when using *Cldn18*-KO mice. (A and B) Images of stomach mucosa stitched together from numerous individual images representing (A) wild-type or (B) *Cldn18*-KO mice after Ussing chamber experiments. Note the variability of mucosal folds that were unable to stretch flat in each tissue. (C) Although the mean length of tissues exceeded the calculated diameter of the CHM2 Ussing chamber opening, which is 9 mm, the length of tissues after Ussing chamber experiments did not differ between wild-type, heterozygous, and *Cldn18*-KO mice. (D and E) Higher magnification images from the inset in (A) and (B), which highlight differences in thickness of gastric mucosa between wild-type (D) and *Cldn18*-KO (E) mice. Single images in (A, B, D, and E) represent observations from $n = 13$ (7 M/6 F) wild-type and $n = 10$ (4 M/6 F) *Cldn18*-KO mouse stomachs. (F) Gastric mucosal height was greater in *Cldn18*-KO compared with both wild-type and heterozygous mice. Results for (C) and (F) were obtained using one-way ANOVA (nonparametric Kruskal-Wallis test) with Dunn's method for post hoc comparisons and are plotted as mean \pm SE from $n = 13$ (7 M/6 F) wild-type, $n = 12$ (6 M/6 F) heterozygous, and $n = 10$ (4 M/6 F) *Cldn18*-KO mouse stomachs evaluated in Ussing chambers. Dotted line represents the mean for each group; female mice are denoted by red dots and male mice with blue dots. L, lumen of the stomach; MM, muscularis mucosa; SM, submucosa. Scale bars: 100 μ m for (D) and (E).

tissues expressing high levels of claudin-2, so we next determined whether claudin-2 protein expression increased concomitant with its mRNA in *Cldn18*-KO mice, and whether the localization of claudin-2 was tight junction associated.

In tissues from *Cldn18*-KO compared with wild-type mice, there was a significant increase in claudin-2 protein expression (Figure 4A and B), with no difference between male or female mice ($P = .394$). Immunostaining for claudin-2 localization was difficult to do because of considerable variability in the antibodies commercially available for this protein. After testing numerous antibodies, we used the mouse monoclonal 12H12 antibody because it was considered to be most reliable of the claudin-2 antibodies commercially available.¹⁹ In FFPE mouse colon, this antibody stained tight junction-associated claudin-2 as expected at the base of crypts (Figure 5), but there was also staining at the basolateral membrane of epithelial cells and strong staining in the subapical cytoplasm of epithelial cells and in the lamina propria that was described as nonspecific in FFPE human

colon tissues.¹⁹ Because tight junctions stained well in FFPE mouse colon, we used tissues prepared similarly from stomach to determine the extent of tight junction localization in *Cldn18*-KO compared with wild-type mice.

Claudin-2 immunostaining of stomach mucosa using FFPE tissues from wild-type mice, which should have little to no claudin-2 expression (Figure 4A), showed robust labeling of claudin-2 with the monoclonal anti-claudin-2 antibody including strong punctate staining between epithelial cells, very bright spots in the lamina propria thought to be nonspecific staining in macrophages,¹⁹ and strong co-localization of claudin-2 with *Griffonia simplicifolia* II lectin-expressing mucous in neck mucous cells that were confirmed to be nonspecific by using *Cldn2*-KO mice (Figure 4C, Figure 6).

Using FFPE tissues from *Cldn18*-KO mice, which had bright spots in the lamina propria but no *Griffonia simplicifolia* II lectin off-target staining, claudin-2 localized to the basolateral membrane and apical supranuclear

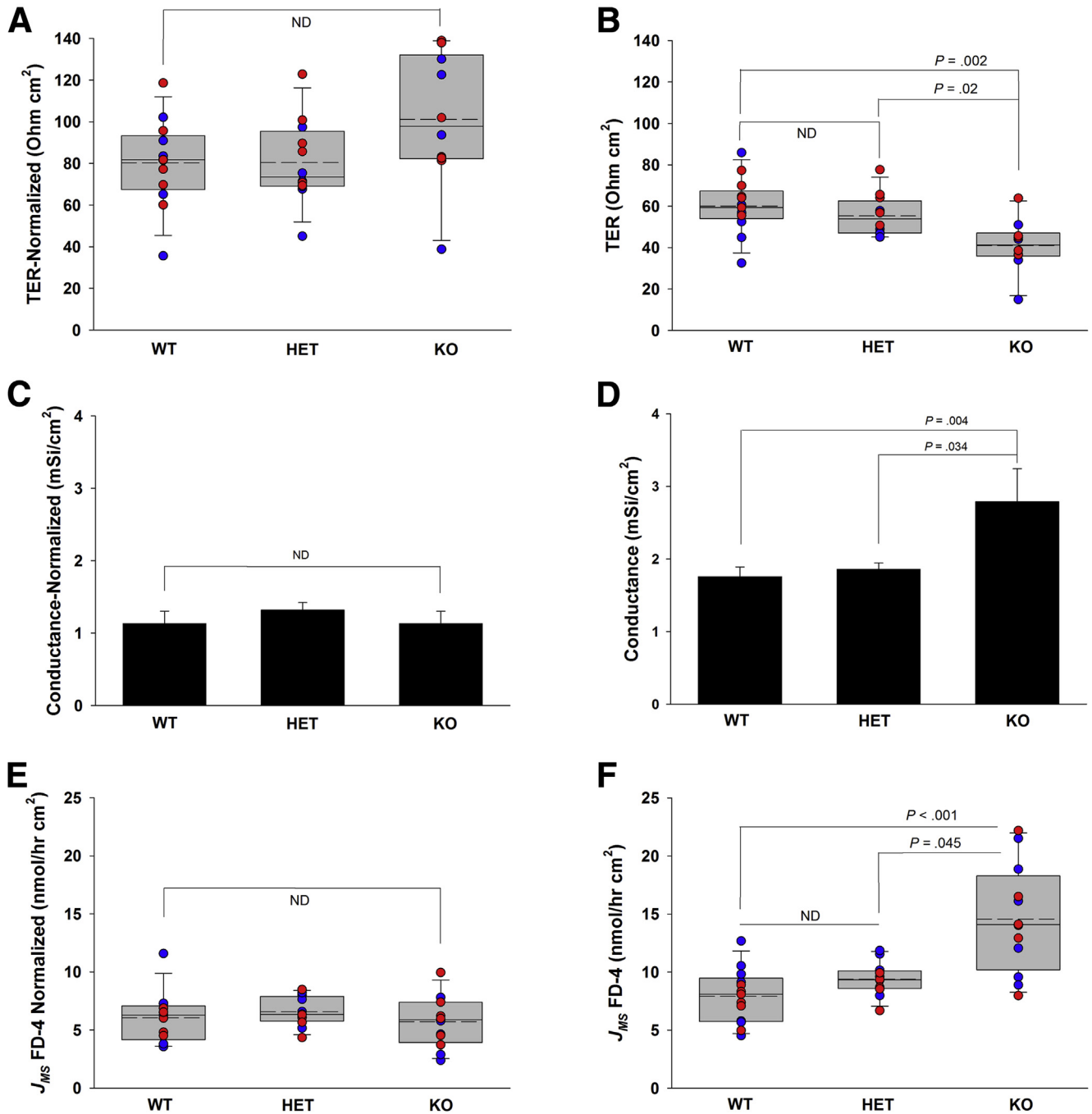
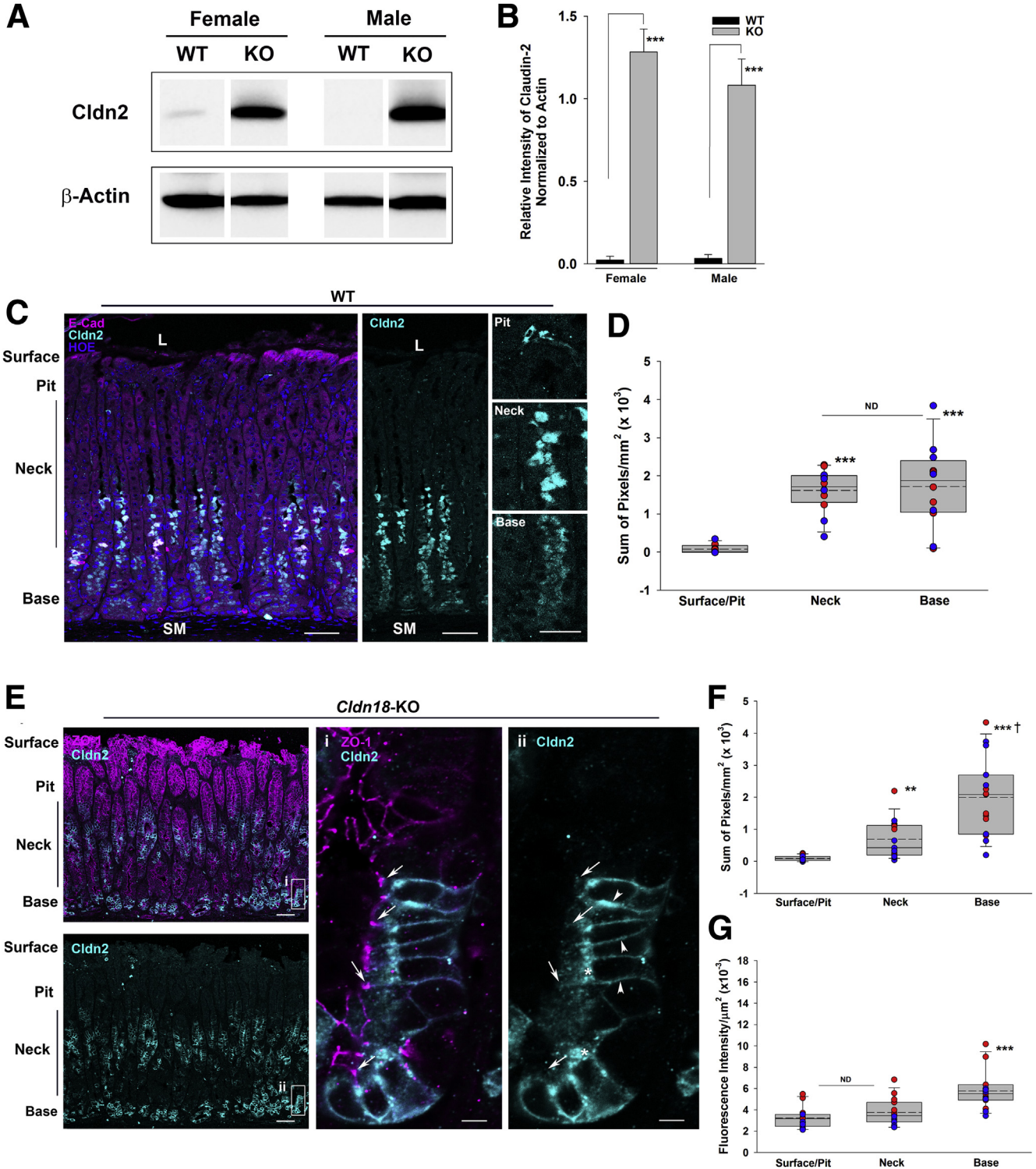


Figure 3. Significant differences in TER, conductance, and mucosal to serosal (J_{MS}) FD-4 flux rates between genotypes are eliminated when mucosal thickness is taken into account. (A–C) When normalized to account for individual differences in tissue height, no significant differences in (A) TER, (B) conductance, or (C) mucosal to serosal FD-4 flux were observed. (D–F) In contrast, when differences in individual tissue height are not taken into consideration when calculating the results, (D) TER in tissues from wild-type and heterozygous mice were significantly higher than in tissues from *Cldn18*-KO mice; (E) tissue conductance in wild-type and heterozygous mice was significantly lower than in *Cldn18*-KO mice; and (F) luminal to basolateral FD-4 flux was significantly higher in *Cldn18*-KO mice when compared with tissues from wild-type or heterozygous mice. Statistical results for all TER and conductance data (normalized and non-normalized) were obtained by using two-way ANOVA with Tukey test for post hoc comparisons and are plotted as means \pm SE from $n = 13$ (7 M/6 F) wild-type, $n = 12$ (6 M/6 F) heterozygous, and $n = 10$ (4 M/6 F) *Cldn18*-KO Ussing preparations. Statistical results for mucosal to serosal FD-4 flux data were determined using Kruskal-Wallis test with Dunn's test for post hoc comparisons and were plotted as means \pm SE from $n = 13$ (7 M/6 F) wild-type, $n = 12$ (6 M/6 F) HET, and $n = 12$ (6 M/6 F) KO Ussing preparations. Statistical results for normalized mucosal to serosal FD-4 flux data were determined using two-way ANOVA with Tukey test for post hoc comparisons and are plotted as means \pm SE from $n = 13$ (7 M/6 F) wild-type, $n = 12$ (6 M/6 F) HET, and $n = 12$ (6 M/6 F) KO Ussing preparations. Dotted line represents the mean for each group; female mice are denoted by red dots and male mice with blue dots. HET, heterozygous.

cytoplasm of epithelial cells. There were infrequent patches of positive cells in the neck region, but most of the positive cells were deep in the gland base (Figure 4E). To quantify this result in tissues from male and female mice, the total amount and the intensity of signal for claudin-2 were

significantly greater in epithelial cells at the base of gastric glands (Figure 4F and G), which did not occur in FFPE tissues from *Cldn2*-KO mice (Figure 6A). This result suggested that claudin-2 expression was localized mainly to epithelial cells in the base of gastric glands and that claudin-2 was not



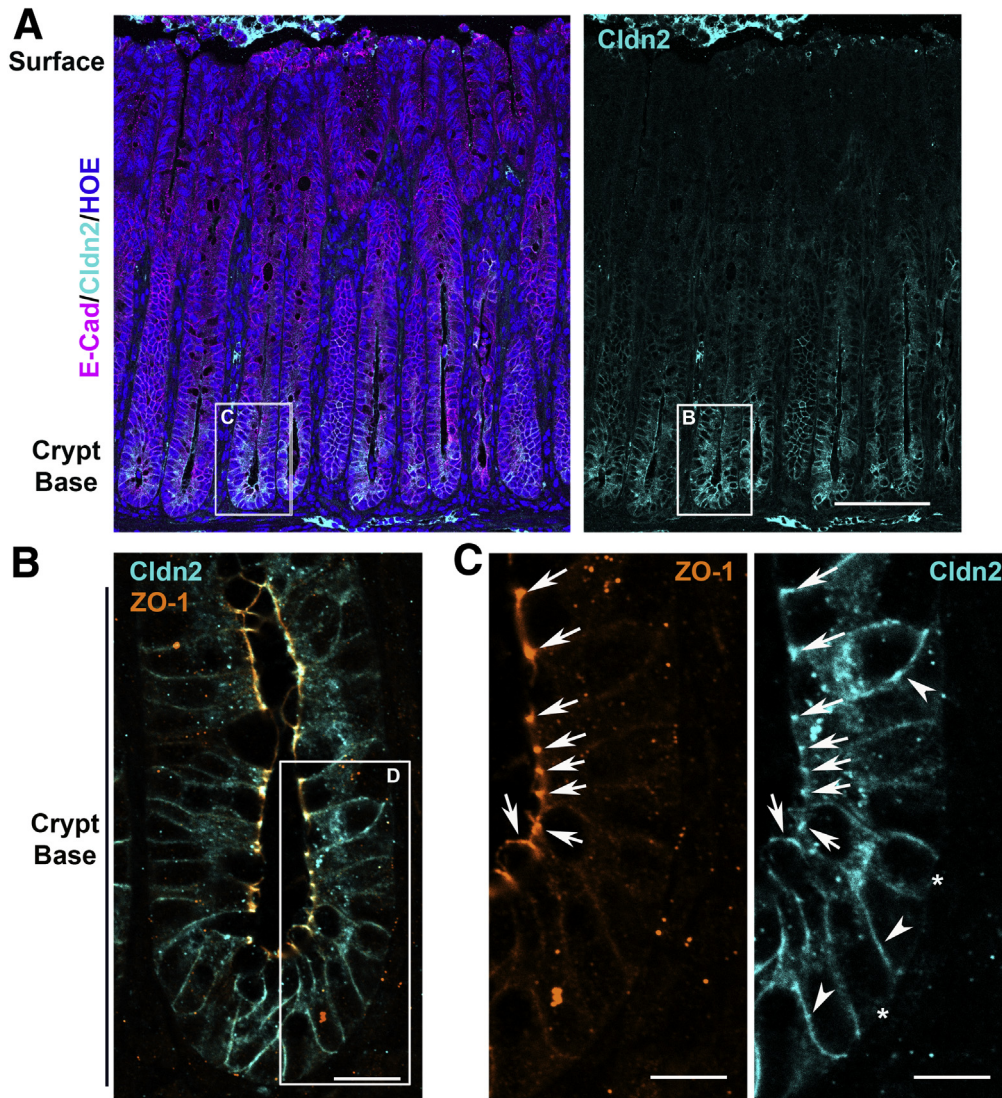


Figure 5. Tight junction expression occurs in colonic mucosa from control mice with claudin-2 antibody; FFPE tissues. (A) Representative images of colonic mucosa from wild-type mice ($n = 3$) stained with E-cadherin (E-cad) antibody to identify lateral cell membranes, claudin-2 (Cldn2) antibody to identify tight junctions, and Hoechst 33342 (HOE) to identify nuclei. As has been determined before in mice,³² in our hands the 12H2 antibody to claudin-2 localized to cells in the crypt base in colon in paraffin sections. (B and C) In the crypt base, claudin-2 co-localized with the tight junction protein ZO-1 (white signal in B, arrows in C) and was also found along the basolateral membrane (arrowheads). Claudin-2 was excluded from the base of cells in colon from FFPE tissues (asterisk). Scale bars: (A) 100 μm ; (B) 20 μm ; (C) 10 μm .

tight junction-associated in FFPE tissues from *Cldn18*-KO mice (Figure 4E).

To address a concern that stomach tight junction organization may not be amenable to FFPE methods, we

immunostained unfixed frozen tissues from wild-type and *Cldn18*-KO mice and analyzed them for co-localization with tight junction zonula occludens 1 (Figure 7A). To provide the most robust analysis of tight junction localization, we used

Figure 4. (See previous page). Increased claudin-2 protein expression in gastric epithelium accompanies up-regulation of *Cldn2* in *Cldn18*-KO mice. (A) Representative claudin-2/actin immunoblot results performed on gastric mucosal tissues. Little claudin-2 is expressed in the normal stomach, whereas there is significant expression in *Cldn18*-KO mice. Single images represent observations from $n = 10$ (5 M/5 F) wild-type and $n = 10$ (5 M/5 F) *Cldn18*-KO mouse stomachs. (B) Quantification of claudin-2 protein expression normalized to actin levels from $n = 10$ (5 M/5 F) wild-type and $n = 10$ (5 M/5 F) *Cldn18*-KO mice confirms significant increase in claudin-2 expression in *Cldn18*-KO mice compared with wild type mice with no effect of sex. *** denotes significance of $P = .001$. (C and D) Confocal microscopy analysis of claudin-2 protein expression in gastric mucosa from wild-type mice ($n = 10$; 5 M/5 F) shows robust claudin-2 expression in FFPE tissues. However, this is nonspecific binding of the antibody to different cells, particularly to mucous in neck mucous cells as confirmed by using similar sections from *Cldn2* knockout mice stained with claudin-2 antibody and *Griffonia simplicifolia* II lectin (Figure 6). Scale bars: 50 μm (low mags), 20 μm (pit, neck, and base insets). Cldn2, claudin-2; E-Cad, E-cadherin; HOE, Hoechst 33342 to stain nuclei; L, gastric lumen; SM, submucosa. (E–G) Confocal microscopy analysis of claudin-2 expression in FFPE tissues from *Cldn18*-KO mice ($n = 10$; 5 M/5 F) shows strong staining in the neck and base with claudin-2 localized to the basolateral membrane. Statistical analysis for pixel sum and fluorescence intensity was obtained using 2-way ANOVA with Tukey test for post hoc comparisons and were plotted as means \pm SE. Scale bars: 50 μm (low mags); 5 μm (insets i and ii). Arrows denote the position of tight junctions. Arrowheads denote the position of basolateral membranes. (D, E, F) ** denotes significance from Surface/Pit at $P = .01$, *** denotes significance from Surface/Pit at $P = .001$, and † denotes significance from Neck at $P = .05$. In B - *** denotes significance of $P = .001$.

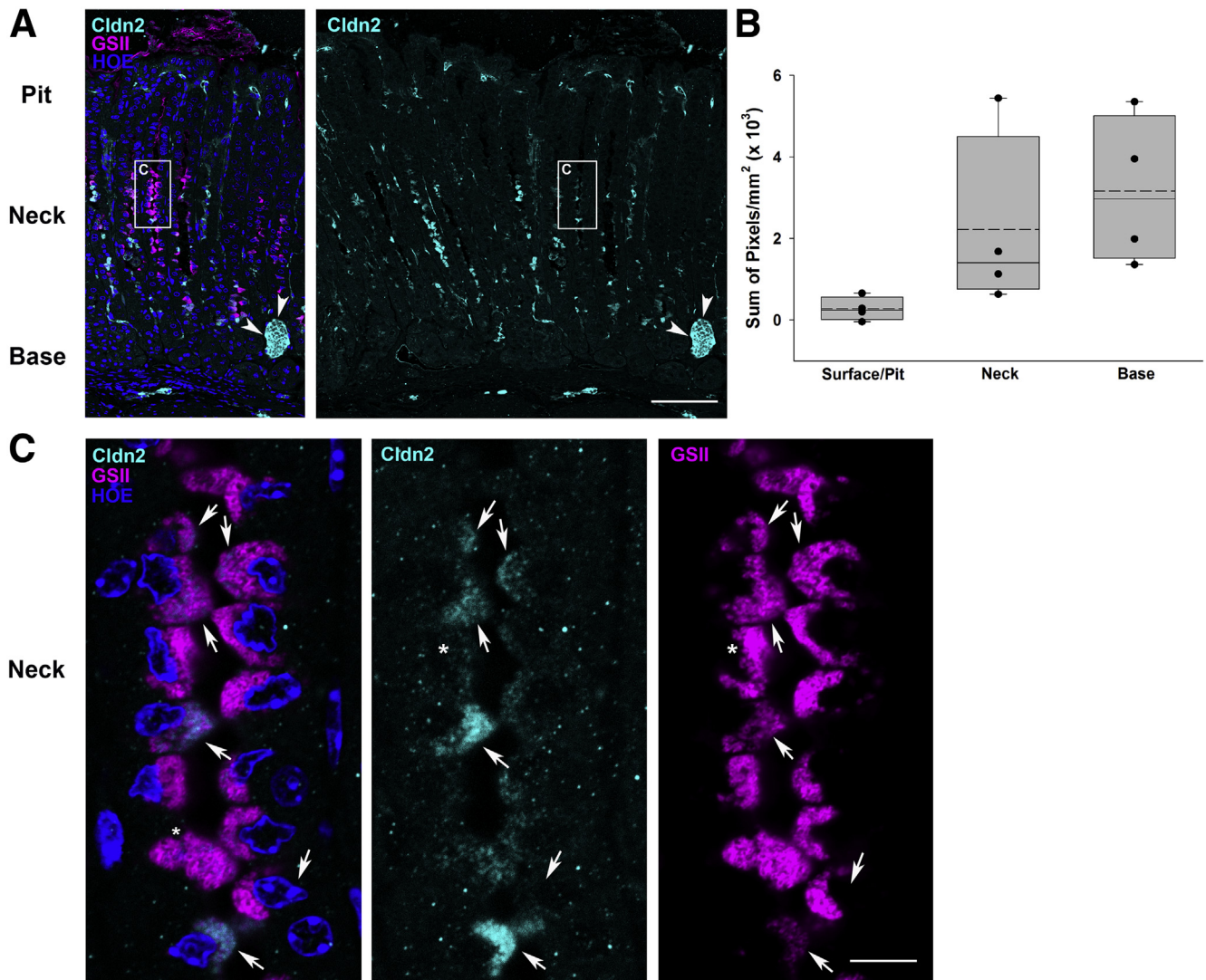


Figure 6. Immunostaining of stomach mucosa from *Cldn2*-deficient (KO) mice results in high background in mucous neck cells with claudin-2 antibody; FFPE tissues. (A) Representative images of corpus mucosa from stomach of male *Cldn2*-KO mice ($n = 2$; 2 M) stained with anti-claudin 2 antibody (Cldn2), GSII lectin from *Griffonia simplicifolia* to identify mucous neck cells, and Hoechst 33342 (HOE) to identify nuclei. Arrowheads indicate a brightly fluorescent structure present in many of the sections and also in sections stained with secondary antibody alone (not shown). Scale bar; 100 μm . (B) Quantification of sum of pixels per area of a specified intensity that were present in the surface, neck, or base. Methods used to quantify the data are identical to Fig. 4C and D. Dotted line represents the mean for each group. One-way ANOVA indicated no differences between groups ($P = .091$), likely because of large variability in neck and base data and low power because of the number of mice used in the analysis. (C) High magnification of the boxed area in (A) shows that the claudin-2 antibody colocalizes with many cells, some of which are also GSII lectin positive (arrows). Some cells are only weakly positive for claudin-2 but have robust expression of GSII lectin (asterisk). Scale bar; 10 μm .

near super-resolution confocal methods (Figure 7B). In frozen sections from wild-type mice, the background staining was significantly reduced, with bright spots still present in the lamina propria and submucosa and some off-target staining in the lamina propria (data not shown). However, tissues from *Cldn18*-KO mice showed basolateral membrane staining and clear but weak claudin-2 associated tight junction staining in cells at the gland base in patches of cells that were positive for claudin-2 (Figure 7A and B). The frozen sections also showed infrequent patches of cells in the neck region that were positive for claudin-2 (Figure 7A). Overall, the data using frozen

sections suggested that claudin-2 is expressed at tight junctions of some cells in the neck and at the gland base of *Cldn18*-KO mice but is most highly localized to the basolateral membrane.

Cldn18 Loss Results in Decreased Transcellular Serosal to Mucosal Chloride Transport

Although TER and FD-4 flux data showed no differences between genotypes (Figure 3A–C), the PD of tissues from wild-type and heterozygous mice differed significantly from

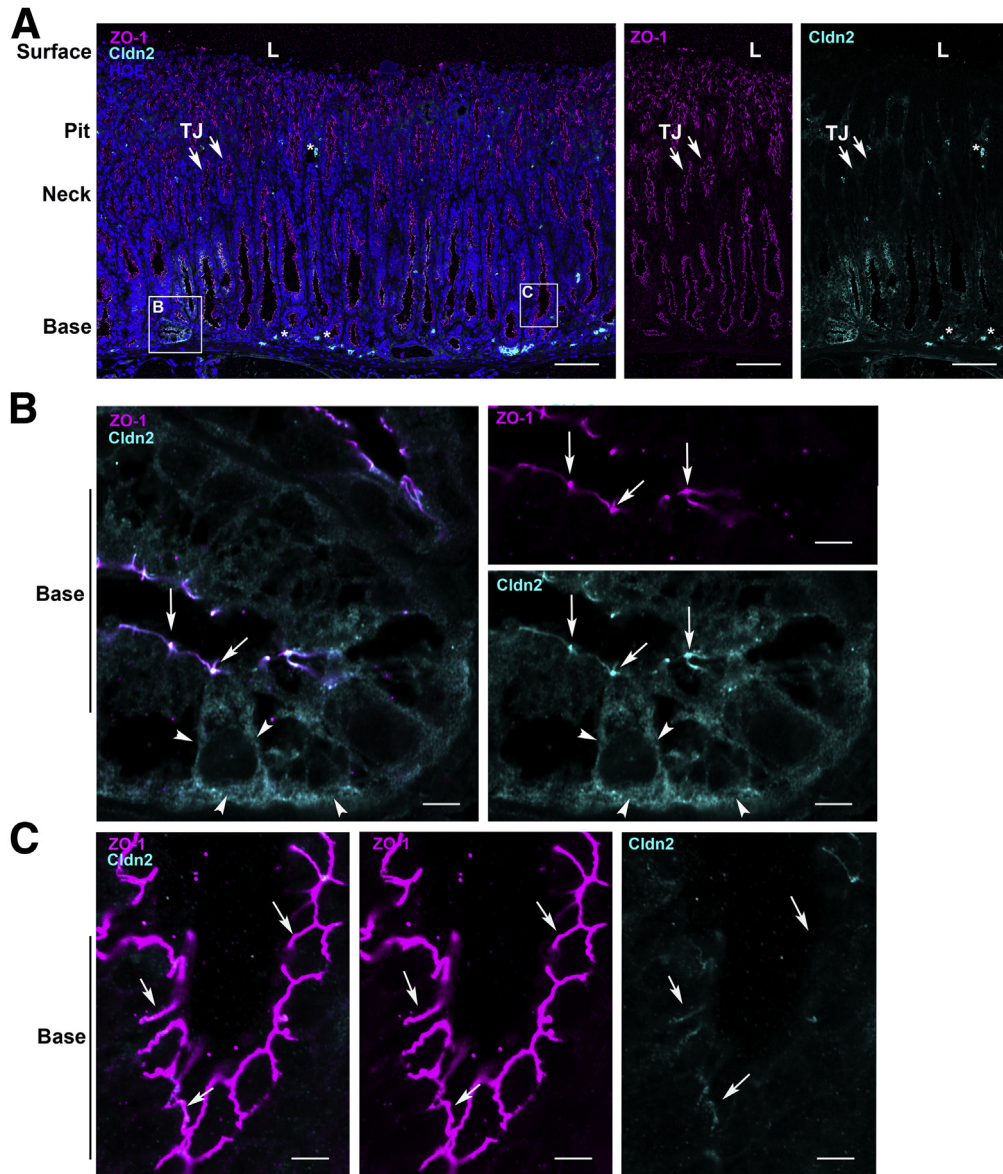


Figure 7. Immunostaining of stomach mucosa from *Cldn18*-deficient (KO) mice shows some tight junction expression with claudin-2 antibody; frozen sections. (A) Representative images of corpus mucosa from stomach of a female *Cldn18*-KO mouse ($n = 6$; 3 M/3 F) stained with mouse anti-claudin 2 (*Cldn2*) antibody 12H2, ZO-1 to identify tight junctions (TJ), and Hoechst 33342 (HOE) to identify nuclei. In frozen sections, claudin-2 localized to cells at base of gastric glands in patchy fashion with areas of relatively strong expression (*inset B*) and most areas with little to no expression (*inset C*). Scale bar, 100 μm . (B) High magnification, near super-resolution images of boxed area in A (*inset B*) shows that claudin-2 is expressed in some glands along the basolateral membrane (*arrowheads*); in addition, it co-localizes with ZO-1 at tight junctions (*arrows*). Scale bar, 5 μm . (C) High magnification, near super-resolution images of boxed area in A (*inset C*) shows that most cells at base of gastric glands have weak to no expression of claudin-2 (*arrows*). Scale bar, 5 μm . L, lumen of the gastric mucosa; asterisks, indicate the position of bright spots (likely macrophages) that are nonspecific staining.

Cldn18-KO mice (Figure 8A). The PD was strongly lumen negative in wild-type and heterozygous mice, whereas the PD was nearly 0 in *Cldn18*-KO mice (Figure 8A). This difference in PD may reflect altered paracellular ion permeability at tight junctions or a significant reduction in transcellular permeability. We measured dilution potentials to determine which pathway was affected in *Cldn18*-KO mice.

Dilution potential experiments showed significantly different Na^+ and/or Cl^- movement in tissues for each

genotype (Figure 8B, $P_{\text{Cl}}/P_{\text{Na}}$). Substitution of NaCl from the mucosal solution resulted in changes in PD (Figure 8C), whereas substitution from the serosal solution did not (Figure 8D). This result alone confirms the lack of tight junction alterations in these mice because tight junctions are passive conduits in which permeability properties are symmetrical (see Discussion). Calculations of absolute permeabilities indicated no significant differences in Na^+ movement between

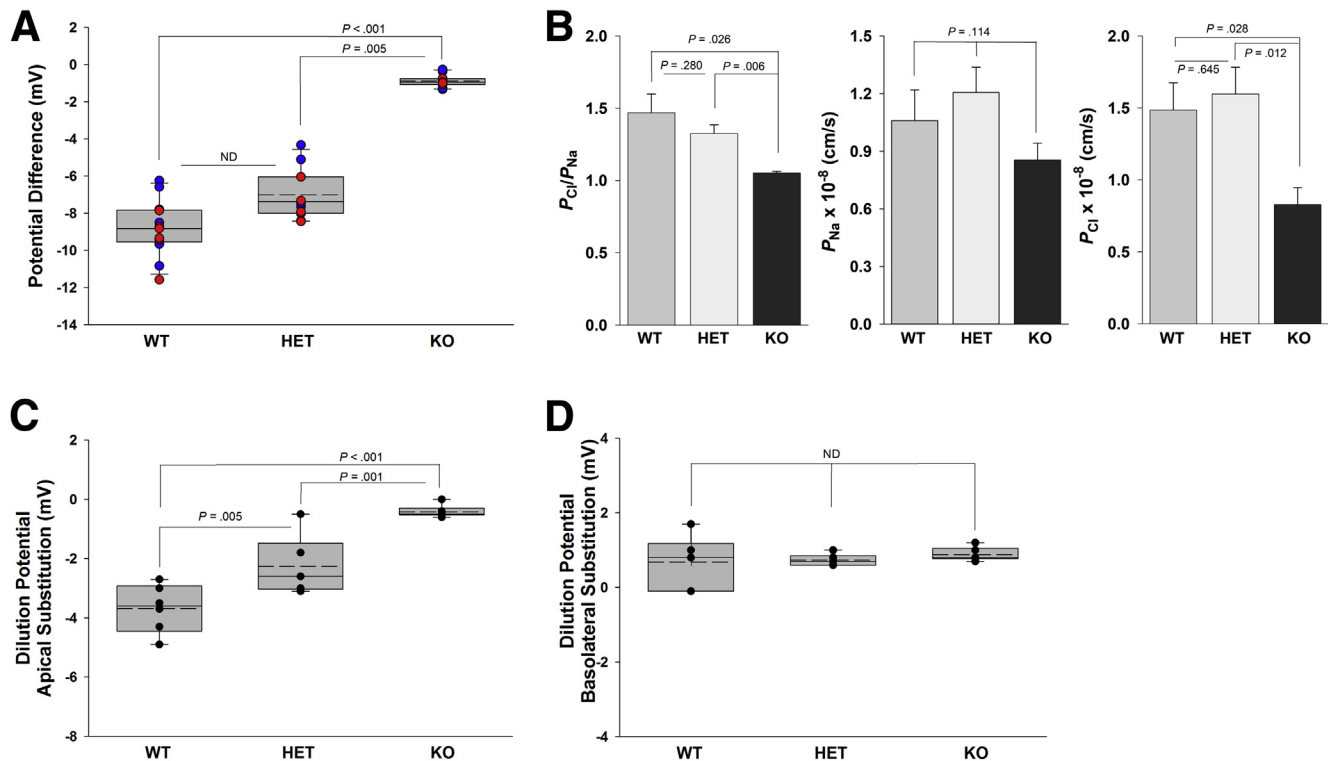


Figure 8. Electrophysiological measurements indicate increased luminal positivity in *Cldn18*-KO mice as a result of decreased basolateral to apical chloride permeability. (A) Stomachs from *Cldn18*-KO mice were characterized by significantly higher (less negative) mean potential differences than stomach from wild-type or heterozygous (HET) mice. (B) P_{Cl}/P_{Na} significantly differed between all groups, attributable to significant reduction in chloride permeability (P_{Cl}) in the stomach from *Cldn18*-KO mice compared with wild-type and heterozygous mice with no differences in sodium permeability (P_{Na}). (C) Significant differences between all groups were observed in dilution potential experiments with apical NaCl substitution. (D) No differences between groups were observed in dilution potential experiments with basolateral NaCl substitution. PD data were determined by using Kruskal-Wallis test with post hoc comparisons performed using Dunn's method and were plotted as means \pm SE from $n = 13$ (7 M/6 F) wild-type, $n = 12$ (6 M/6 F) HET, and $n = 12$ (6 M/6 F) KO Ussing preparations. Dilution potential (basolateral NaCl substitution) data were determined by using Kruskal-Wallis test and are plotted as means \pm SE from $n = 6$ (3 M/3 F) Ussing preparations per genotype. Dilution potential (apical NaCl substitution) data were determined by using one-way ANOVA with post hoc comparisons performed by using Tukey test and were plotted as means \pm SE from $n = 6$ (3 M/3 F) Ussing preparations per genotype. P_{Cl} and P_{Na} results were calculated by using the Goldman-Hodgkin-Katz and Kimizuka-Koketsu equations, with statistical analysis performed using one-way ANOVA with post hoc comparisons with Tukey test and were plotted as means \pm SE from $n = 6$ (3 M/3 F) Ussing preparations per genotype. Dotted line in box plots represents the mean for each group; female mice are denoted by red dots and male mice with blue dots.

genotypes (Figure 8B, P_{Na}), whereas Cl^- movement was significantly slower in *Cldn18*-KO compared with wild-type and heterozygous mice (Figure 8B, P_{Cl}). These results suggest that an anion transport deficit exists in *Cldn18*-KO mice that is not tight junction associated but is rather a defect in transcellular chloride transport in a serosal to mucosal direction. With sodium movement unchanged, the slower rate of chloride movement results in neutralization of the charge and thus a near-zero PD in tissues from *Cldn18*-KO mice.

Loss of *Cldn18* Results in the Down-Regulation of Major Chloride Transporters in the Gastric Mucosa of *Cldn18*-KO Mice

Our genomic database annotated numerous genes encoding proteins for neck cell region chloride transporters, many of which differ significantly in *Cldn18*-KO compared

with wild-type mice (Figure 9). When further separated into ion transporters located at the basolateral membrane (used for Cl^- loading), we observed that *Slc4A2* (AE2) was down-regulated, whereas *Slc12A2* (NKCC1) was unchanged (Figure 9A and B). In addition, *Slc12A6* (KCC3a), an ion transporter that binds to the sodium potassium adenosine triphosphatase (NaK-ATPase), targets it to lipid raft domains on the basolateral membrane, and regulates its activity,²⁰ was down-regulated (Figure 9A and B). Ion transporters used for Cl^- secretion at the apical membrane include *Clcn2* (ClC-2) and *Cftr*, which were up-regulated, whereas *Slc26A9* and *Slc12A7* (KCC4) were down-regulated (Figure 9A and B).

We previously showed that *Cftr* localized to the apical membrane of metaplastic cells in the gland base from *Cldn18*-KO mice.¹⁵ For the mucosa to secrete Cl^- into the gastric lumen, NKCC1 must be targeted to the basolateral membrane for Cl^- loading. We thus confirmed that NKCC1

targeted to the basolateral membrane of cells at the base of metaplastic glands in *Cldn18*-KO mice (Figure 9C). This localization was not typical, because NKCC1 targeted to the basolateral membrane of parietal and neck cells in wild-type mice and not to gland base cells (Figure 9D). NKCC1 membrane targeting is regulated by phosphorylation via Wnk/Spak/Osr1,^{21,22} for which the mRNA expression (*P* values were calculated for Log2 data) was not different in *Cldn18*-KO vs wild-type mice (Figure 9E). For NKCC1 to function in Cl⁻ loading, the NaK-ATPase must also localize to the basolateral membrane in *Cldn18*-KO mice to create an ion gradient. We thus confirmed that NaK-ATPase targeted to the basolateral membrane of cells at the base of metaplastic glands in *Cldn18*-KO mice (Figure 9F). However, parietal cells in the mucosa from *Cldn18*-KO mice had abnormal expression of NaK-ATPase along the basolateral membrane (Figure 9F, inset i), resembling internalization and/or glycosylation defects described previously.²³ Furthermore, NaK-ATPase was homogeneously localized along the basolateral membrane in metaplastic cells (Figure 9F, inset ii), which was similar to chief cells (Figure 9G, inset ii). This localization pattern was in distinct contrast to the basolateral membrane localization in parietal and neck cells from wild-type mice, which was “beaded” along the entire membrane (Figure 9G, inset i). These data demonstrate that major ion transporters for Cl⁻ loading and Cl⁻ secretion localize to a compartment consistent with supporting Cl⁻ secretion in *Cldn18*-KO mice but that the subcellular organization is not the same in metaplastic compared with wild-type cells.

Discussion

Although it is unclear how *Cldn18* loss causes progressive neoplasia development, one hypothesis is that permeability defects result in inflammation and mucosal damage to start the cancer cascade. This concept was supported by data using *stCldn18*-KO mice, which showed cytokine up-regulation, mucosal injury, and metaplasia development as a result of barrier defects caused by the loss of stomach-specific claudin-18.¹¹ In contrast, using different methods of analysis and a different mouse model, namely a global *Cldn18*-deficient mouse, our work demonstrates that (1) global *Cldn18* loss in mice at 7 weeks after birth does not cause tight junction dysfunction or alter paracellular permeability; (2) despite changes in claudin gene expression that should result in impaired cation specificity at tight junctions, mucosa from mice lacking claudin-18 show deficient transcellular Cl⁻ permeability that may be due to changes in the expression or activity of apical and basolateral transporters for Cl⁻ loading and Cl⁻ secretion, respectively; and (3) *Cldn18* loss results in a number of significant structural alterations in the gastric mucosa, such as the loss of parietal cells, that impact ion conductance and thus require consideration when analyzing physiological data from *Cldn18*-KO mice.

TER and solute permeability, studied in Ussing chambers, are dependent on cell geometry,^{2,24} emphasizing the

importance of identifying relevant histopathology when studying these parameters in genetically altered mice. Differences in surface area (cell number/mucosal height) and tight junction length, for instance, are not typically considered when using a monolayer of epithelial cells grown on Transwell filters that are structurally the same. However, in tissues from *Cldn18*-KO mice, a significant increase in cell number per area¹⁵ increases cell-cell contact length per area that permits the passage of solutes and electrical current.^{2,24} The increase in cell number/cell-cell contact length per area would theoretically increase paracellular permeability and decrease TER, which likely explains our results without normalization. Thus, significant changes in cell geometry occur in the stomach mucosa of *Cldn18*-KO mice that require consideration when calculating electrophysiological data.

An additional geometric consideration when using ex vivo mouse stomach tissues in Ussing chambers is that they are not flat, but rather they assume a half-ellipsoid shape if taken from across the greater curvature. It is necessary to use stomach mucosa from across the greater curvature to fill the entire Ussing chamber opening because the mouse stomach is small. Even when stretching the stomach, the mounted mucosa is a half-ellipsoid rather than flat. This means that in comparison to cells grown on Transwell filters, the surface area cannot be calculated from the radius of the chamber opening but instead using surface area measurements of a half-ellipsoid. We discovered that this calculation needed to be performed individually for each tissue because of variability in stretch, with the resultant surface area used in calculations of the electrophysiological measurements for that tissue.

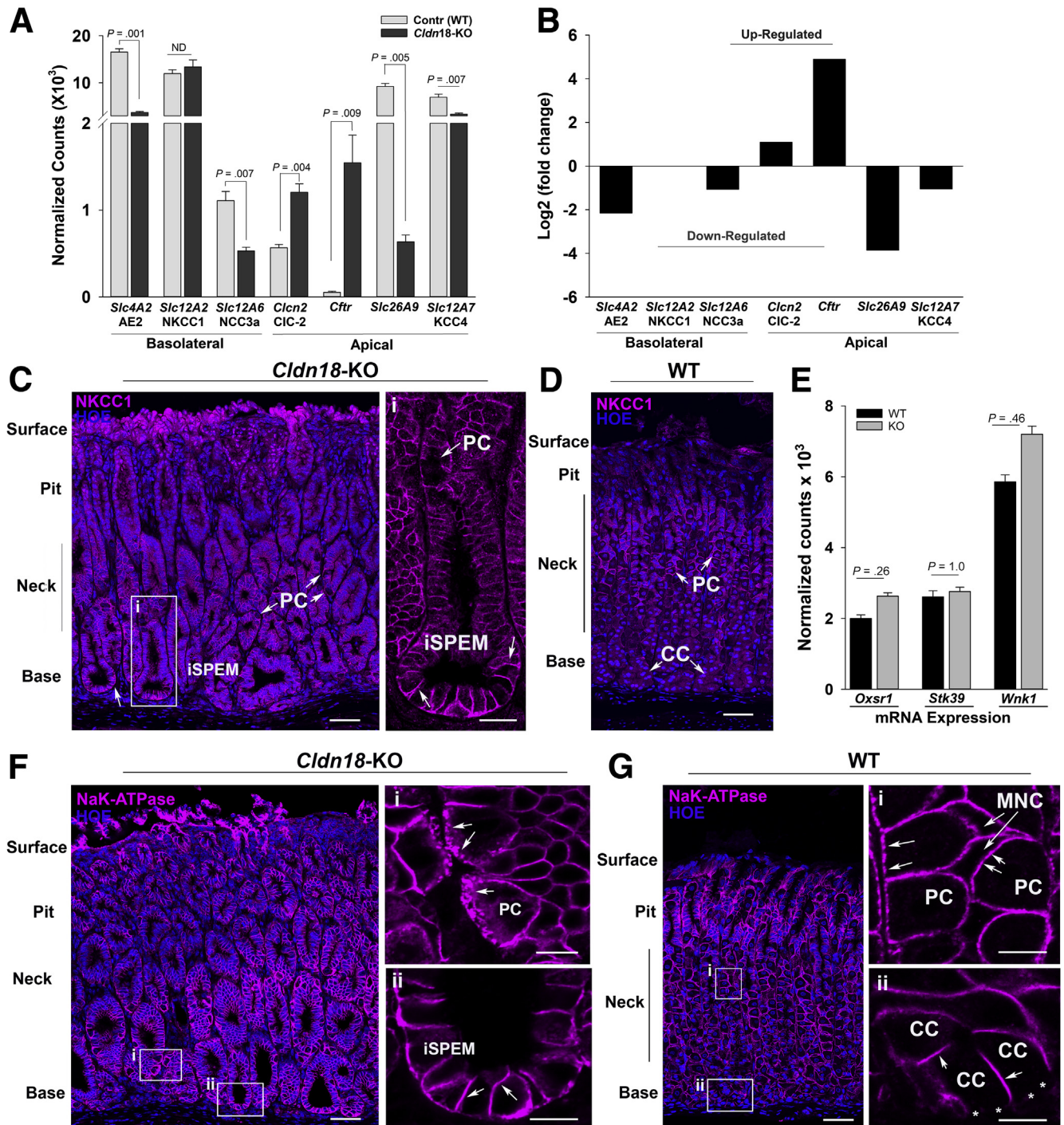
Forte and Machen²⁵ showed that when the mammalian stomach ex vivo is incubated with identical solutions facing mucosal and serosal surfaces, such as we had here, there was a spontaneous electrical PD, with the mucosal solution negative with respect to the serosal solution. In the case of stomach mucosa from wild-type and heterozygous mice in our study, this PD was -8.83 mV. PD is generated in the mammalian stomach by active sodium transport in the mucosal to serosal direction that is offset by chloride transport in the serosal to mucosal direction. In the case of gastric mucosa from wild-type and heterozygous mice in our study, mean Na⁺ permeability was less than Cl⁻ permeability, thus generating a net negative PD. In contrast, mean Na⁺ permeability was not different from Cl⁻ permeability in *Cldn18*-KO mice, resulting in little PD across the mucosa. Of interest is why Cl⁻ permeability was slower in *Cldn18*-KO mice.

Recent computer modeling studies indicate that additional geometric characteristics impact predicted ion conductances in the stomach including the location of parietal cells (distance from the bathing solution), the presence of parietal cell canaliculi, the number of gastric glands per linear centimeter, length and diameter of the gland lumen, and the distance of the gland lumen from the bathing solution.²⁶ If any of these parameters are different in genetically altered mice, differences in ion transport mechanisms and/or tissue conductance may occur and be due solely to changes in geometry.²⁶ In addition to increased mucosal

height/cell number, *Cldn18*-KO mice show nearly complete mucosal atrophy (no parietal cells) by 7 weeks after birth.¹⁵ Because parietal cells are thought to dominate the total ion conductance of the gastric mucosa,^{26,27} ion secretion in mouse tissues from *Cldn18*-KO mice with atrophy should have altered electrical parameters, as well as Cl^- , Na^+ , and K^+ transcellular flux compared with wild-type mice.

Although Na^+ and Cl^- transport can occur via paracellular or transcellular routes, dilution potential results

with mucosal versus serosal NaCl substitution in our study were asymmetric, indicating changes in transcellular and not paracellular permeability.²⁸ With the specific changes in claudin expression that occurred in *Cldn18*-KO mice, including the down-regulation of claudins-8 and -15 and the up-regulation of claudin-2, all changes that would generate a significant Na^+ permeability across the mucosa, it would be easy to argue that the near-zero PD was due to high levels of Na^+ permeation through tight junctions that offset Cl^-



movement across the mucosa. However, permeability calculations showed that Cl^- , rather than Na^+ , permeability was affected in our model. This result is in contrast to an increase in both Na^+ and Cl^- permeabilities previously reported in *stCldn18-KO* mice.¹¹ Although *Cldn18-KO* mice do not express lung claudin-18 at tight junctions,¹⁵ making them different from *stCldn18A2.1-KO* mice,¹¹ one potential difference is that we corrected all permeability measurements for individual tissue surface area and normalized to mucosal height.

In the mouse stomach, transcellular ion secretion is either acidic, which occurs during agonist-stimulated acid secretion, or nonacidic.²⁶ Because we used famotidine to inhibit stimulated acid secretion in all tissues, TER and PD measurements in wild-type mice represent the situation for nonacidic electrogenic ion secretion. However, gene profiling of the corpus mucosa from *Cldn18-KO* mice demonstrated that at 7 weeks after birth, genes typically found in the antrum rather than corpus are expressed,¹⁵ suggesting that secretions in the same region from wild-type and *Cldn18-KO* mice would be different. In the corpus mucosa, 2 major Cl^- loading transporters are basolateral in parietal cells; one is *Slc4A2* (AE2), which is a $\text{Cl}^-/\text{HCO}_3^-$ exchanger, and the other is *Slc12A2* (NKCC1), which is a Na^+ , K^+ , 2Cl^- co-transporter.²⁶ AE2, a specific parietal cell marker that is mainly involved in Cl^- loading during acid secretion,²⁶ is down-regulated at the mRNA and protein level in *Cldn18-KO* mice because of parietal cell loss.¹⁵ NKCC1 is the dominant basolateral pathway for Cl^- loading in parietal cells that are involved in nonacidic electrogenic ion secretion and in Cl^- secretion from mucous cells in the antral gland base.²⁹ For NKCC1 to function as a co-transporter, low intracellular Na^+ has to be generated by the proper membrane targeting and activation of the NaK-ATPase. Aided by KCC3a in parietal cells, an isoform of the K^+-Cl^- cotransporter, the NaK-ATPase is transported into distinct lipid-raft domains along the basolateral membrane, which significantly increases its

ATPase activity.²⁰ KCC3 mRNA and protein were down-regulated in metaplastic cells from *Cldn18-KO* mice, and concomitantly the NaK-ATPase was localized homogeneously along the basolateral membrane rather than to distinct membrane structures (beading) as we showed here in parietal cells. This result suggests that NaK-ATPase activity may be reduced, thus reducing serosal to mucosal Na^+ , K^+ , and Cl^- flux and providing a potential mechanism for the altered rate of Cl^- flux in *Cldn18-KO* mice. This reduction in Cl^- flux would occur despite the up-regulation of *Cftr* at the apical membrane of cells at the gland base in *Cldn18-KO* mice.¹⁵ Thus, *Cldn18-KO* mice express apical and basolateral transporters to facilitate Cl^- secretion, but because of parietal cell loss, changes in geometry, a reduced Na^+ gradient, or other factors are unable to transport Cl^- in excess of Na^+ to maintain a negative lumen in the resting state. Because deficits in ion transporter expression and function can be associated with gastric cancer development or progression,³⁰ further experiments should be done to examine the relationship between ion transporters and the phenotype of *Cldn18-KO* mice.

In summary, this study demonstrates that in contrast to current thinking, barrier defects at tight junctions are not likely an adult phenotype after the loss of claudin-18. This result is important because it suggests that progressive neoplasia development in *Cldn18-KO* mice is initiated by factors other than permeability defects that drive inflammation and mucosal injury. Because claudin-18 is mainly a basolateral membrane protein, our results also suggest that it does not function as an accessory pore protein to augment tight junction function in adult tissues but instead may organize cellular signaling or have some other function in cells that is required for cellular homeostasis. Because the loss of *CLDN18* expression is associated with the development of gastric cancer in human patients, determining how it regulates gastric homeostasis and pathways affected by its loss may inform

Figure 9. (See previous page). Loss of *Cldn18* results in dysregulation of gastric mucosal chloride transporter expression. (A) mRNA expression for gastric mucosal chloride transporters that (A) normally display a specific basolateral or apical distribution pattern and (B) significantly differed (Log_2 , $P < .0001$) between tissues from wild-type and *Cldn18-KO* mice in the RNASeq analysis. Normalized counts data were determined by using Kruskal-Wallis test with post hoc comparisons performed using Dunn's method and are plotted as means \pm SE from $n = 3$ (3 M) wild-type and $n = 3$ (3 M) *Cldn18-KO* mice. (C) Confocal microscopy analysis of NKCC1 expression and localization in tissues from *Cldn18-KO* mice ($n = 4$; 2 M/2 F) shows strong membrane localization in intestinalized SPEM cells (iSPEM) at base of gastric glands, a position that was shown to express *Cftr*.¹⁵ Inset (i) is higher magnification image of the gland base to better show NKCC1 localization. HOE, Hoechst 33342 to identify nuclei; PC, parietal cells. Scale bars: 50 μm (low mag); 20 μm (inset i). (D) Confocal microscopy analysis of NKCC1 expression and localization in tissues from wild-type mice ($n = 4$; 2 M/2 F) shows strong membrane localization along the basolateral membrane of PC with no membrane localization in chief cells (CC) at the base of gastric glands. Scale bar: 50 μm . (E) mRNA expression for effectors that regulate NKCC1 in tissues from wild-type and *Cldn18-KO* mice. P values represent the Log_2 -fold change in expression between wild-type and *Cldn18-KO* mice. (F) Confocal microscopy analysis of NaK-ATPase expression and localization in tissues from *Cldn18-KO* mice ($n = 4$; 2 M/2 F) shows strong membrane localization in iSPEM at the base of gastric glands. Inset (i) is higher magnification image of PC, demonstrating thickened signal along the basolateral membrane (arrows). At the gland base, NaK-ATPase localizes in a homogeneous manner to the basolateral membrane of iSPEM cells (arrows). Scale bars: 50 μm (low mag); 10 μm (insets i and ii). (G) Confocal microscopy analysis of NaK-ATPase expression and localization in tissues from wild-type mice ($n = 4$; 2 M/2 F) shows strong membrane localization in all cells in the gastric corpus mucosa. Inset (i) is higher magnification image of PC and neck mucous cells (MNC), demonstrating a beaded localization of signal along the basolateral membrane (arrows). In contrast, NaK-ATPase localizes in a homogeneous manner to the basolateral membrane of CCs (arrows). Note that in CCs, NaK-ATPase does not localize to the basal membrane (asterisks). Scale bars: 50 μm (low mag); 10 μm (insets i and ii).

the development of new therapeutic treatments for gastric cancer.

Materials and Methods

Mice

B6;129S5-CLDN18^{tm1Lex}/Mmucd mice were purchased as frozen embryos from the Mutant Mouse Resource and Research Center (Davis, CA) and re-derived, bred, and housed at Massachusetts Institute of Technology (MIT) in an Association for Assessment and Accreditation of Laboratory Animal Care International approved facility. For each experiment, equal numbers of male and female wild-type, heterozygous, or *Cldn18*-KO mice were used at 7 weeks of age. Genotyping was performed by Transnetyx (Cordova, TN) via ear punches taken at weaning. Rapid cervical dislocation was used as a method of euthanasia to minimize tissue hypoxia. Alternative methods, such as the use of CO₂ euthanasia, result in more extended periods of tissue hypoxia, which are not suitable for maintaining maximum tissue viability during setup and throughout experiments. Animal experiments were performed according to institutional guidelines, and the animal protocol was approved by the Committee on Animal Care at MIT.

Stomach tissues from *Cldn2*-deficient mice^{31,32} were provided by Dr Sachiko Tsukita, Osaka University, Japan.

Reagents and Antibodies

FD-4, tetrodotoxin, indomethacin, and famotidine were purchased from Sigma-Aldrich (St Louis, MO). Mouse anti-claudin-2 antibody (12H12; Invitrogen, Carlsbad, CA; cat #32-5600), raised against 26 amino acids at the C-terminus, was purchased from Thermo Fisher Scientific (Rockford, IL), rat anti-ZO-1 was made by Dr Daniel Goodenough, and rabbit anti-E-cadherin antibody (AF648) was purchased from R&D Systems (Minneapolis, MN). Tetrodotoxin was purchased and used according to institutional guideless with a protocol approved by the MIT Biosafety Office.

Tissue Preparation and Ussing Chamber Setup

After euthanasia, the stomach was rapidly excised, opened along the lesser curvature, and gently washed in ice-cold Ringer's solution (containing in mmol/L: 145.5 NaCl, 4 KCl, 1.2 CaCl₂, and 0.05 indomethacin) to remove the stomach contents. The stomach was pinned mucosal side down on a thick Sylgard 184 (Sigma-Aldrich) plate, covered with ice-cold Ringer's solution that was continuously gassed with 100% O₂, and the muscularis externa was removed from the underlying mucosa using a stereomicroscope as described previously.^{29,33} Tissues were then mounted between 2 Lucite halves of a Ussing-type chamber with an exposed mucosal area of 0.636 cm², with care taken to exclude mucosa from the squamous forestomach and antrum. In all Ussing chamber experiments, luminal and serosal sides of the tissue were bathed with a solution containing (in mmol/L): 108 NaCl, 22 NaHCO₃, 3 KCl, 1.3 MgSO₄, 2 CaCl₂, 2.25 KH₂PO₄, 8.9 glucose, 10 Na-pyruvate, 0.03 indomethacin, 0.001 tetrodotoxin, and 0.3 famotidine (pH 7.4), and continuously gassed with 95% O₂-5%

CO₂.^{33,34} Indomethacin and tetrodotoxin were used to inhibit prostaglandins and to abolish neuronal influences in mammalian stomach, respectively.^{33,34} Institutional approval was obtained for the use of tetrodotoxin, which is a federal select agent toxin that is regulated by the Centers for Disease Control and Prevention. Famotidine, a histamine H₂ receptor antagonist, was used to block gastric acid secretion because acid secretion drives transepithelial electrical characteristics of the gastric epithelium.^{26,27} The sum of interventions using indomethacin, tetrodotoxin, and famotidine was important to minimize variation to ensure reproducible transepithelial electrical data that could be interpreted between genotypes. After the completion of experiments, stomach tissues were fixed in 10% neutral buffered formalin (Thermo Fisher Scientific, Hampton, NH) and processed for paraffin histology by the Beth Israel Deaconess Medical Center Histology core.

Electrophysiological Measurements

Measurements of PD and TER from male (n = 5–6) and female (n = 5–6) mice from each genotype were monitored by KCl-saturated agar bridges connected via 2 calomel electrodes to a voltmeter. TER was calculated from Ohm's law using the change in voltage between mucosal and serosal sides during the application of a 50 μ A current every 5 minutes. Five consecutive measurements of PD and TER were taken at 30-minute intervals, beginning 1.25 hours after mounting, after all electrical parameters were stabilized. TER and PD values are reported as the average of these 5 measurements.

Flux Measurements

Fluorescein isothiocyanate-labeled FD-4 (1 mg/mL) was added to the mucosal side, and 1 mL of sample was collected from the serosal side every 30 minutes with replacement using unlabeled buffer. Flux measurements were taken in conjunction with TER and PD from male and female mice from each genotype above. Samples were analyzed using a Spectromax M5 spectrophotometer (Molecular Devices, Sunnyvale, CA). FD-4 concentration was calculated from a standard curve. Flux rates were calculated from the slope of linear regression equation determined by plotting FD-4 concentration versus time.

Dilution Potentials, Calculation of P_{Cl}/P_{Na} , and Calculation of Absolute Permeabilities

In separate experiments, tissues from male (n = 5–6) and female (n = 5–6) mice from each genotype were mounted and allowed to equilibrate in the chamber for 1.25 hours, after which both sides were drained of buffer. The basolateral side was refilled with nutrient buffer, and the luminal side was filled with an osmotically balanced buffer solution that contained (in mmol/L): 54 NaCl, 3 KCl, 22 NaHCO₃, 1.3 MgSO₄, 108 mannitol, 2.25 KH₂PO₄, 10.0 Na-pyruvate, 0.001 tetrodotoxin, 0.03 indomethacin, 2 CaCl₂, 8.9 dextrose, and 0.3 famotidine, pH 7.4 (from here forward referred to as dilution buffer). After substitution, PD and TER values were recorded immediately and then twice at 15-minute intervals.

After this, both chamber sides were drained and filled with nutrient buffer. After a 30-minute equilibration period, the substitution process was repeated, with nutrient buffer in the luminal side and dilution buffer in the basolateral side. Respective luminal and basolateral dilution potential values were calculated as the difference between PD recorded immediately before and 30 minutes after buffer substitution (V in the equation below). P_{Cl}/P_{Na} values were calculated by using the Goldman-Hodgkin-Katz equation for dilution potentials,^{35,36} and absolute permeabilities were determined by using the Kimizuka-Koketsu equation as described by Yu et al^{37,38} as follows:

$$x = e^{-VF/RT}$$

$$P_{Cl}/P_{Na} = \beta = \frac{\alpha - x}{\alpha x - 1}$$

$$P_{Na} = G \cdot \left(\frac{RT}{F^2} \right) / (a(1 + \beta))$$

$$P_{Cl} = P_{Na} \cdot \beta$$

e = Mathematical constant, 2.71828

V = Dilution potential, calculated as described above.

G = Tissue conductance (1/TER) per unit surface area

α = Activity ratio. The calculated activity of NaCl in the dilution buffer divided by the calculated activity of NaCl in the nutrient buffer

a = Na^+ activity in nutrient buffer. This number is the same as the activity of NaCl in the nutrient buffer.³⁷

F = Faraday constant (96,485.3329 C/mol)

R = Ideal Gas constant (8.314 J/mol K)

T = Temperature (310.15° K).

Activity coefficients first require conversion of molarity to molality and then extrapolating the activity coefficient at 37°C from Trusdell.³⁹ At 37°C, 108 mmol/L NaCl is 0.109 molal, and the activity coefficient is 0.774175. Thus, the calculated activity of NaCl at 108 mmol/L is 0.0844. Likewise at 37°C, 54 mmol/L NaCl is 0.05417 molal, and the activity coefficient is 0.8155. Thus, the calculated activity of NaCl at 54 mmol/L is 0.0442. All TER/conductance measurements used in these calculations were first normalized to individual mucosal thickness, as described above.

Surface Area Determination

Mouse stomach in our study was not flat when mounted on a Ussing chamber. Instead, it was naturally curved so that the surface area represented that of an oblate spheroid (ellipsoid) divided in half along the 2-dimensional plane defined by the symmetrical axes, a and b (Figure 10A), where a is the x-axis and b is the y-axis. The fixed radius values of the symmetrical axes (a , b) were defined by the size of the chamber opening, which was 0.45 cm (CHM2 chamber diameter was 9 mm). Eqn 1 (Figure 10B) is Ramanujan's second approximation,^{40,41} and Eqn 2 (Figure 10C) was modified by us from the Knud-Thomsen

approximation of ellipsoid surface area.⁴² Eqn 2 (Figure 10C) defines the surface area of a half-ellipsoid, SA_{tissue} , which describes the relationships between all 3 axial radii, the ellipsoid equatorial perimeters, and the half-ellipsoid surface area. A measurement of the semi-circumference around the asymmetrical plane defined by the axes a and c (" d " in Figure 10A) was obtained for each experimental tissue and used in Eqn 1 (Figure 10B) to determine the radius of the asymmetrical axis c (Figure 10A), which was subsequently used in Eqn 2 (Figure 10C) to determine the tissue surface area.

Measurement of " d "

After fixation, tissues were halved along the 2-dimensional plane defined by the axis a (Figure 10A), embedded in paraffin, and cut along the long axis. After sectioning and staining with H&E, digital images were taken along the entire length using an Axioimager wide-field microscope system (Carl Zeiss AG, Oberkochen, Germany) and then stitched into one image by using FUJI software (Tokyo, Japan). The final image was measured from end to end, and the total length was calculated by using ImageJ software.

Measurements of Mucosal Thickness

Using the stitched images, mucosal height (measured from the base of gastric glands to the mucosal surface) was measured at 5 equidistant positions along the length. The average height per tissue was calculated and used for normalization. In preliminary data, the number of cells per height was quantified by staining tissues with DAPI (to identify nuclei), and Volocity Image Processing Software (Quorum Technologies, Puslinch, Ontario, Canada) was used to calculate the number of cells per area as described by Hagen et al.¹⁵ Because height measurements were correlated to cell number (data not shown), all measurement corrections were done using mucosal height.

Confocal Microscopy and Image Analysis

Antigen retrieval using citrate buffer, pH 6.0, was used on paraffin sections from male ($n = 5$) or female ($n = 5$) *Cldn18-KO* or wild-type mice or from *Cldn2-KO* mice ($n = 2$, male) before staining with mouse anti-claudin-2 (Invitrogen 32-5600) and rat anti-ZO-1 (obtained from Dr Goodenough) or rabbit anti-E cadherin (R&D Systems, AF648), followed by secondary antibodies with complementary probes. Frozen sections were stained with the same antibodies after blocking for nonspecific staining in male ($n = 3$) or female ($n = 3$) *Cldn18-KO* mice or ($n = 2$) wild-type mice. Claudin-2 was always imaged in far red to reduce background staining. The same strategy was used for paraffin sections from male ($n = 2$) or female ($n = 2$) wild-type or *Cldn18-KO* mice stained with anti-NKCC1 (LSBio, Seattle, WA; LS-C313276-100) or anti-NaK-ATPase (Abcam, Cambridge, UK; ab76020 [EP1845Y]). Sections were mounted in Prolong Gold anti-fade mounting medium containing Hoechst 33342 (Invitrogen) to stain nuclei and evaluated by using an LSM880 confocal system with or without Fast Airyscan (Carl Zeiss).

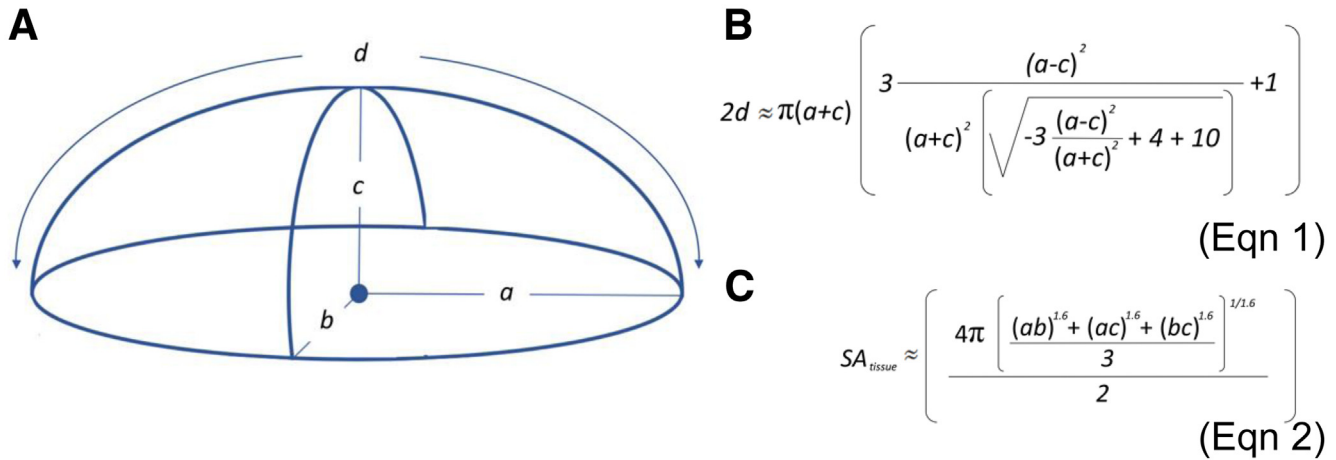


Figure 10. Diagram and equations for surface area determinations. (A) Schematic diagram of an oblate semi-spheroid (ellipsoid). For this geometric structure, a , b , and c are semi-axes, and d is the tissue length (see Figure 2). This model was used to calculate surface area for Ussing chamber experiments where a was the radius along the x-axis, b was the radius along the y-axis, and c was the radius along the z-axis. For tissues mounted in the chambers, $a = b =$ radius of the chamber, d was calculated as in Figure 2, and c was determined from Eqn 1. (B) Eqn 1 is Ramanujan's second approximation.^{40,41} (C) Eqn 2 was modified from the Knud-Thomsen approximation of ellipsoid surface area and defines the surface area of a semi-ellipsoid.⁴² SA_{tissue} describes the relationships between all 3 axial radii, the ellipsoid equatorial perimeters, and the half-ellipsoid surface area.

The sum of pixels that were positive for claudin-2 was quantified using Volocity image analysis software. For this, two $\times 20$ image tiles (3×2) from each tissue section were used. Within each image, 3 separate regions of interest were defined for analysis: (1) the surface and gastric pit, (2) the neck region, and (3) the gland base region. The sum of pixels within a specified intensity range with exclusion of background was collected and normalized to area. Likewise, the average pixel intensity per region of interest was quantified.

Western Blotting and Protein Quantification

Gastric mucosal samples were collected from male ($n = 5$) and female ($n = 5$) wild-type or *Cldn18-KO* mice. After excision, stomachs were opened along the greater curvature and washed in ice-cold phosphate-buffered saline. The mucosa was scraped into pre-weighed cryotubes on ice, taking care to exclude the esophagus, antrum, and duodenum. Directly after scraping, tubes containing tissue were weighed and immediately frozen in liquid nitrogen, followed by storage at -80°C .

To prepare gel samples, each mucosal sample was transferred into a Dounce homogenizer containing 9 volumes of ice-cold sample buffer containing (in mmol/L) 150 Tris-Cl, 2 EDTA, 0.1% sodium dodecyl sulfate, 1% sucrose containing Complete Mini protease inhibitor (Roche Biosciences, Indianapolis, IN) as described previously.⁴³ Determination of protein levels was carried out using the Bio-Rad Protein Assay kit (Bio-Rad, Hercules, CA). Proteins were resolved by 12% sodium dodecyl sulfate–polyacrylamide gel electrophoresis and transferred to polyvinylidene difluoride membranes. The blots were incubated with mouse anti-claudin-2 (1/1000), followed by washing and incubation with secondary horseradish peroxidase conjugated anti-mouse (1/3000), and the signal

was imaged by chemiluminescence using a Bio-Rad Chemidoc Imaging System (Bio-Rad). Membranes were stripped, washed, and reincubated with primary antibody (mouse anti-actin, 1/10,000) as a loading standard. Normalization and quantification of claudin-2 protein levels were carried out using Bio-Rad Image Lab Software v. 5.2.1 (Bio-Rad).

Preparation of RNA and RNASeq

Tissues from wild-type (male, $n = 3$) or *Cldn18-KO* (male, $n = 3$) mice at 7 weeks after birth were frozen (unfixed) in optimal cutting temperature medium and prepared for RNASeq analysis as described in detail.¹⁵ Normalization was done during the bioinformatics pipeline analysis to convert raw read counts into measures of gene expression.

Statistical Analyses

Data were analyzed by one-way or two-way analysis of variance (ANOVA), followed by post hoc comparisons using SigmaPlot 14 software (Systat Software, San Jose, CA). Analysis of variance on ranks was performed if variances were not equal. Outliers were identified using the ROUT method at $Q = 1\%$ (GraphPad Software, San Diego, CA). Outlying data were omitted from analysis and graphs. Graphs were produced by using SigmaPlot 14 software. The data were considered significant at $P < .05$.

All authors had access to the data and reviewed and approved the final manuscript.

References

1. Tsukita S, Furuse M, Itoh M. Multifunctional strands in tight junctions. *Nat Rev Mol Cell Biol* 2001;2:285–293.

2. Anderson JM, Van Itallie CM. Physiology and function of the tight junction. *Cold Spring Harb Perspect Biol* 2009; 1:a002584.
3. Krug SM, Schulzke JD, Fromm M. Tight junction, selective permeability, and related diseases. *Semin Cell Dev Biol* 2014;36:166–176.
4. Van Itallie CM, Anderson JM. Architecture of tight junctions and principles of molecular composition. *Semin Cell Dev Biol* 2014;36:157–165.
5. Turner JR. Intestinal mucosal barrier function in health and disease. *Nat Rev Immunol* 2009;9:799–809.
6. Tamura A, Yamazaki Y, Hayashi D, Suzuki K, Sentani K, Yasui W, Tsukita S. Claudin-based paracellular proton barrier in the stomach. *Ann N Y Acad Sci* 2012; 1258:108–114.
7. Günzel D, Yu AS. Claudins and the modulation of tight junction permeability. *Physiol Rev* 2013; 93:525–569.
8. Suzuki H, Tani K, Tamura A, Tsukita S, Fujiyoshi Y. Model for the architecture of claudin-based paracellular ion channels through tight junctions. *J Mol Biol* 2015; 427:291–297.
9. Tsukita S, Tanaka H, Tamura A. The claudins: from tight junctions to biological systems. *Trends Biochem Sci* 2019;44:141–152.
10. Hagen SJ. Non-canonical functions of claudin proteins: beyond the regulation of cell-cell adhesions. *Tissue Barriers* 2017;5:e1327839.
11. Hayashi D, Tamura A, Tanaka H, Yamazaki Y, Watanabe S, Suzuki K, Suzuki K, Sentani K, Yasui W, Rakugi W, Isaka Y, Tsukita S. Deficiency of claudin-18 causes paracellular H⁺ leakage, up-regulation of interleukin-1-beta, and atrophic gastritis in mice. *Gastroenterology* 2012;142:292–304.
12. Suzuki K, Sentani K, Tanaka H, Yano T, Suzuki K, Oshima M, Yasui W, Tamura A, Tsukita S. Deficiency of stomach-type claudin-18 in mice induces gastric tumor formation independent of *H pylori* infection. *Mol Cell Gastroenterol Hepatol* 2019;8:119–142.
13. Wroblewski LE, Shen L, Ogden S, Romero-Gallo J, Lapierre LA, Israel DA, Turner JR, Peek RM. *Helicobacter pylori* dysregulation of gastric epithelial tight junctions by urease-mediated myosin II activation. *Gastroenterology* 2009;136:236–246.
14. Wroblewski LE, Peek RM, Wilson KT. *Helicobacter pylori* and gastric cancer: factors that modulate disease risk. *Clin Microbiol Rev* 2010;23:713–739.
15. Hagen SJ, Ang LH, Zheng Y, Karahan SN, Wu J, Wang YE, Caron TJ, Gad AP, Muthupalani S, Fox JG. Loss of tight junction claudin 18 promotes progressive neoplasia development in mouse stomach. *Gastroenterology* 2018;155:1852–1867.
16. Sanada Y, Oue N, Mitani Y, Yoshida K, Nakayama H, Yasui W. Down-regulation of the claudin-18 gene, identified through serial analysis of gene expression data analysis, in gastric cancer with an intestinal phenotype. *J Pathol* 2006;208:633–642.
17. Matsuda Y, Semba S, Ueda J, Fuku T, Hasuo T, Chiba H, Sawada N, Kuroda Y, Yokozaki H. Gastric and intestinal claudin expression at the invasive front of gastric carcinoma. *Cancer Sci* 2007;98:1014–1019.
18. Amasheh S, Meiri N, Gitter AH, Schöneberg T, Mankertz J, Schulzke JD, Fromm M. Claudin-2 expression induces cation-selective channels in tight junctions of epithelial cells. *J Cell Sci* 2002;115:4969–4976.
19. Randall K, Henderson N, Reens J, Eckersley S, Nyström A-C, South MC, Balendran CA, Böttcher G, Hughes G, Price SA. Claudin-2 expression levels in ulcerative colitis: development and validation of an *in situ* hybridisation assay for therapeutic studies. *PLoS One* 2016;11:e0162076.
20. Fujii T, Takahashi Y, Itomi Y, Fujita K, Morii M, Tabuchi Y, Asano S, Tsukada K, Takeguchi N, Sakai H. K⁺-Cl⁻ cotransporter-3a up-regulates Na⁺,K⁺-ATPase in lipid rafts of gastric luminal parietal cells. *J Biol Chem* 2008; 283:6869–6877.
21. Dorwart MR, Shcheynikov N, Wang Y, Stippec S, Muallem S. SLC26A9 is a Cl(-) channel regulated by the WNK kinases. *J Physiol* 2007;584:333–345.
22. Mercier-Zuber A, O'Shaughnessy KM. Role of SPAK and OSR1 signalling in the regulation of NaCl cotransporters. *Curr Opin Nephrol Hypertens* 2011;20:534–540.
23. Vagin O, Tokhtaeva E, Sachs G. The role of the beta1 subunit of the Na,K-ATPase and its glycosylation in cell-cell adhesion. *J Biol Chem* 2006; 281:39573–39587.
24. Marcial MA, Carlson SL, Madara JL. Partitioning of paracellular conductance along the ileal crypt-villus axis: a hypothesis based on structural analysis with detailed consideration of tight junction structure-function relationships. *J Membr Biol* 1984;80:59–70.
25. Forte JG, Machen TE. Transport and electrical phenomena in resting and secreting piglet gastric mucosa. *J Physiol* 1975;244:33–51.
26. Carothers JM, Forte JG, Machen TE. Computer modeling of the gastric parietal cell: significance of the canalicular space, gland lumen, and variable canalicular [K⁺]. *Am J Physiol Gastrointest Liver Physiol* 2018; 310:G671–G681.
27. Rehm WS, Schwartz M, Carrasquer G. Direct current electrical measurements in epithelia: steady-state and transient analysis. *Methods Enzymol* 1989; 171:607–628.
28. Van Itallie CM, Rahner C, Anderson JM. Regulated expression of claudin-4 decreases paracellular conductance through a selective decrease in sodium permeability. *J Clin Invest* 2001;107:1319–1327.
29. McDaniel N, Pace AJ, Spiegel S, Engelhardt R, Koller BH, Seidler U, Lytle C. Role of Na-K-2Cl cotransporter-1 in gastric secretion of non-acidic fluid and pepsinogen. *Am J Physiol Gastrointest Liver Physiol* 2005;289:G550–G560.
30. Yuan D, Ma Z, Tuo B, Li T, Liu X. Physiological significance of ion transporters and channels in the stomach and pathophysiological relevance in gastric cancer. *Evid Based Complement Alternat Med* 2020;2020:2869138.
31. Wada M, Tamura A, Takahashi N, Tsukita S. Loss of claudins 2 and 15 from mice causes defects in paracellular

- Na⁺ flow and nutrient transport in gut and leads to death from malnutrition. *Gastroenterology* 2013;144:369–380.
32. Tsai P-Y, Zhang B, He W-Q, Zha J-M, Odenwald MA, Singh G, Tamura A, Shen L, Sailer A, Yeruva S, Kuo W-T, Fu Y-X, Tsukita S, Turner JR. IL-22 upregulates epithelial claudin-2 to drive diarrhea and enteric pathogen clearance. *Cell Host Microbe* 2017; 21:671–681.
 33. Song P, Groos S, Riederer B, Feng Z, Krabbenhöft A, Manns MP, Smolka A, Hagen SJ, Neusch C, Seidler U. Kir4.1 channel expression is essential for parietal cell control of acid secretion. *J Biol Chem* 2011; 286:14120–14128.
 34. Schulzke JD, Gitter AH, Mankertz J, Spiegel S, Seidler U, Amasheh S, Saitou M, Tsukita S, Fromm M. Epithelial transport and barrier function in *occludin*-deficient mice. *Biochim Biophys Acta* 2005; 1669:34–42.
 35. Barry PH. The reliability of relative anion-cation permeabilities deduced from reversal (dilution) potential measurements in ion channel studies. *Cell Biochem Biophys* 2006;46:143–154.
 36. Cerejido M, Robbins ES, Dolan WJ, Rotunno CA, Sabatini DD. Polarized monolayers formed by epithelial cells on a permeable and translucent support. *J Cell Biol* 1978;77:853–880.
 37. Yu AS, Cheng MH, Angelow S, Günzel D, Kanzawa SA, Schneeberger EE, Fromm M, Coalson RD. Molecular basis for cation selectivity in claudin-2-based paracellular pores: identification of an electrostatic interaction site. *J Gen Physiol* 2008;133:111–127.
 38. Kimizuka J, Koketsu K. Ion transport through cell membrane. *J Theoret Biol* 1964;6:290–305.
 39. Truesdell AH. Activity coefficients of aqueous sodium chloride from 15° to 50° C measured with a glass electrode. *Science* 1968;161:884–886.
 40. Aghera R, Desai H, Sharma P, Dholakiya N, Agrawal N. Maxillary and mandibular arch perimeter prediction using Ramanujan's equation for the ellipse-*in vitro* study. *Br J Med Med Res* 2016;17:1–9.
 41. Ramanujan S. Modular equations and approximations to π . *Quart J Math* 1914;45:350–372.
 42. Xu D, Cui J, Bansal R, Hao X, Liu J, Peterson BS. The ellipsoidal area ratio (EAR): an alternative anisotropy index for diffusion tensor imaging. *Magn Reson Imaging* 2009;27:311–323.
 43. Hagen SJ, Yanaka A, Jansons R. Localization of brush border cytoskeletal proteins in gastric oxynticopeptic cells from the bullfrog *Rana catesbeiana*. *Cell Tissue Res* 1994;275:255–267.

Received February 12, 2020. Accepted October 13, 2020.

Correspondence

Address correspondence to: Susan J. Hagen, PhD, Department of Surgery, E/RW-871, Beth Israel Deaconess Medical Center, 330 Brookline Avenue, Boston, Massachusetts 02115. e-mail: shagen@bidmc.harvard.edu; fax: (617) 975-5562.

Acknowledgments

The authors thank Professor Ursula Seidler for advice on running mouse tissues in Ussing chambers and Professor Sachiko Tsukita for allowing us to use the *Cldn2* knockout mice that were developed in her laboratory.

CRedit Authorship Contributions

Tyler J. Caron, DVM (Conceptualization: Supporting; Data curation: Lead; Formal analysis: Lead; Investigation: Lead; Methodology: Equal; Validation: Lead; Writing – original draft: Supporting; Writing – review & editing: Supporting)

Kathleen E. Scott, DVM (Methodology: Equal)
Nishita Sinha (Data curation: Supporting; Formal analysis: Equal; Investigation: Supporting; Validation: Supporting)

Sureshkumar Muthupalani, DVM, PhD (Formal analysis: Lead)

Baqai Mahnoor, MD (Investigation: Lead)

Lay-Hong Ang, PhD (Investigation: Supporting; Methodology: Lead)

Yue Li, PhD (Investigation: Supporting)

Jerrold R. Turner, MD, PhD (Data curation: Supporting; Formal analysis: Equal; Resources: Supporting; Writing – review & editing: Supporting)

James G. Fox, DVM (Conceptualization: Supporting; Funding acquisition: Supporting; Project administration: Supporting; Resources: Supporting; Supervision: Supporting; Writing – review & editing: Supporting)

Susan J. Hagen, PhD (Conceptualization: Lead; Data curation: Supporting; Formal analysis: Supporting; Funding acquisition: Lead; Investigation: Supporting; Methodology: Supporting; Project administration: Lead; Resources: Lead; Supervision: Lead; Writing – original draft: Lead)

Conflicts of interest

This author discloses the following: JRT is a cofounder of and shareholder in Thelium Therapeutics. The remaining authors disclose no conflicts.

Funding

Supported by the Harvard Catalyst | The Harvard Clinical and Translational Science Center, National Center for Research Resources, and the National Center for Advancing Translational Sciences, National Institutes of Health (NIH) award 1UL1 TR001102-01, and financial contributions from Harvard University and its affiliated academic health care centers, Department of Surgery Bridge funds, and NIH grants R01 DK103046 and P30 DK034854 (S.J.H.); NIH grants R01 CA093405, P30 ES002109, R35CA21088, and P01CA028842 (J.G.F.); NIH and DOD grants R01DK068271, R01DK061931, and DOD CDMRP PR181271 (J.R.T.); and a Research Science Institute/Center for Excellence in Education Summer Research Fellowship (N.S.). T.J.C. and K.E.S. were supported by NIH T32 OD0109978 (J.G.F.).